Geochemistry, Geophysics, Geosystems®

RESEARCH ARTICLE
10.1029/2023GC011086

Africa's Crustal Architecture Inferred From Probabilistic and Perturbational Inversion of Ambient Noise: ADAMA

Tolulope Olugboji[1,2,3], **Siyu Xue**[1,3], **Jean-Joel Legre**[1], **and Yuri Tamama**[1,4,5]

[1]Department of Earth and Environmental Sciences, University of Rochester, Rochester, NY, USA, [2]Department of Electrical and Computer Engineering, University of Rochester, Rochester, NY, USA, [3]Georgen Institute of Data Sciences, University of Rochester, Rochester, NY, USA, [4]Department of Geosciences, Princeton University, Princeton, NJ, USA, [5]Seismological Laboratory, California Institute of Technology, Pasadena, CA, USA

Abstract Africa's continental crust hosts a variety of geologic terrains and is crucial for understanding the evolution of its longest-lived cratons. However, few of its seismological models are yet to incorporate the largest continent-wide noise dispersion data sets. Here, we report on new insights into Africa's crustal architecture obtained using a new data set and model assessment product, ADAMA, which comprises a large ensemble of short-period surface wave dispersion measurements: 5–40 s. We construct a continent-wide model of *A*frica's *C*rust *E*valuated with ADAMA's *R*ayleigh *P*hase maps (*ACE-ADAMA-RP*). Dispersion maps, and uncertainties, are obtained with a probabilistic approach. This model update, and a crustal taxonomy derived from unsupervised machine learning, reveals that the architecture of Africa's crust can be classified into two main types: *primitive* (C1: faster velocities with little gradients) and *modified* (C2–C4: slower velocities in the shallow crust with more pronounced gradients). The Archean shields are "primitive," showing little variation or secular evolution. The basins, orogens, and continental margins are "modified" and retain imprints of surface deformation. The crustal taxonomy is obtained without a-priori geological information and differs from previous classification schemes. While most of our reported features are robust, probabilistic modeling suggests caution in the quantitative interpretations where illumination is compromised by low-quality measurements, sparse coverage or both. Future extension of our approach to other complementary seismological and geophysical data sets—for example, multimode earthquake dispersion, receiver functions, gravity, and mineral physics, will enable continent-wide lithospheric modeling that extends resolution to the upper mantle.

Plain Language Summary The rocks that constitute Africa's crust record the history of different geological periods. We produce a map, for the entire continent, of how fast shear waves travel within these rocks. We obtain this map from ambient noise surface wave vibrations. The ambient noise surface waves are generated from ocean and atmospheric waves that couple with the solid Earth. There are two types: Rayleigh and Love waves and they travel at different speeds for different wavelengths. This property is called dispersion and it is used to tell how fast the shear wave speeds travel within the subsurface rocks. Constructing the final map from ambient noise surface waves requires the solution of a computational imaging problem. We solve the most challenging computational task with a probabilistic approach—using random sampling—and this enables us to also construct associated error maps. The new maps of Africa's crust show new features that have important implications for subsurface geology of the continent.

Key Points:

- A continent-wide s-velocity model of Africa's crust is constructed using probabilistic modeling of the largest catalog of dispersion measurements
- A crustal taxonomy, derived with unsupervised machine learning, reveals that Africa's crust is one-third primitive and two-thirds modified
- Archean shields are primitive and show no secular evolution; basins, orogens, and margins are modified, retaining imprints of deformation

Supporting Information:

Supporting Information may be found in the online version of this article.

Correspondence to:

T. Olugboji,
tolugboj@ur.rochester.edu

Citation:

Olugboji, T., Xue, S., Legre, J.-J., & Tamama, Y. (2023). Africa's crustal architecture inferred from probabilistic and perturbational inversion of ambient noise: ADAMA. *Geochemistry, Geophysics, Geosystems*, *24*, e2023GC011086. https://doi.org/10.1029/2023GC011086

Received 8 JUN 2023
Accepted 1 NOV 2023

Author Contributions:

Conceptualization: Tolulope Olugboji
Data curation: Tolulope Olugboji, Siyu Xue, Jean-Joel Legre, Yuri Tamama
Formal analysis: Tolulope Olugboji, Siyu Xue, Yuri Tamama
Funding acquisition: Tolulope Olugboji
Investigation: Tolulope Olugboji, Yuri Tamama
Methodology: Tolulope Olugboji

1. Introduction

The African continent possesses many geological terrains and tectonic features of great interest, including multiple cratons spanning billions of years in age (Begg et al., 2009; Jessell et al., 2016), a long-wavelength superswell topography in the south (Lithgow-Bertelloni & Silver, 1998; Fishwick & Bastow, 2011), active and failed continental rifts (Chorowicz, 2005; Min & Hou, 2019), hotspots and active volcanoes and multiple second-order basins and swells (Burke & Gunnell, 2008; Doucouré & de Wit, 2003) (Figure 1a). One approach to studying the diverse and spatially undersampled regions of Africa's bulk crust is to turn to seismic velocity models (Adams & Nyblade, 2011; Emry et al., 2019; Pasyanos et al., 2014). These models provide useful constraints on the composition of the crust (Hacker et al., 2012; Rudnick & Gao, 2014; Sammon et al., 2022), the identification of structural boundaries within and across different tectonic domains (Buehler & Shearer, 2017) and how rheology (Shinevar et al., 2015, 2018) and density (Haas et al., 2020, 2021; Molinari & Morelli, 2011) influence continental rifting, isostatic and dynamic uplift, long-term deformation, and seismicity within the African plate (Behn

Project Administration: Tolulope Olugboji
Resources: Tolulope Olugboji, Siyu Xue, Jean-Joel Legre, Yuri Tamama
Software: Tolulope Olugboji, Siyu Xue, Yuri Tamama
Supervision: Tolulope Olugboji
Validation: Tolulope Olugboji
Visualization: Tolulope Olugboji, Siyu Xue, Jean-Joel Legre, Yuri Tamama
Writing – original draft: Tolulope Olugboji
Writing – review & editing: Tolulope Olugboji

et al., 2002; Borrego et al., 2018; Fadel et al., 2020; Lowry & Pérez-Gussinyé, 2011; Schmandt et al., 2015; Schutt et al., 2018; White-Gaynor et al., 2021).

Insight into Africa's crust is provided by global (Laske et al., 2013; Pasyanos et al., 2014), as well as continent-wide velocity models (Adams & Nyblade, 2011; Begg et al., 2009; Fadel et al., 2020; Fishwick & Bastow, 2011; Li & Burke, 2006; Nair et al., 2006; Yang et al., 2008). A selection of the continent-wide seismic velocity models published in the last decade include Litho1.0 (Laske et al., 2013; Pasyanos et al., 2014), Africa.ANT. Emry-etal.2018 (Emry et al., 2019; Trabant et al., 2012), AF2019 (Celli, Lebedev, Schaeffer, & Gaina, 2020), and SA2019 (Celli, Lebedev, Schaeffer, Ravenna, & Gaina, 2020). All of these models are replicas of CRUST1.0 (Laske et al., 2013; Pasyanos et al., 2014) in the shallowest crust, except for Litho1.0, a heavily cited global velocity model, which updates CRUST1.0 by incorporating earthquake-derived surface wave dispersion measurements (Laske et al., 2013; Pasyanos et al., 2014). Taken together, these models include both active and passive source data sets, but are yet to fully integrate comprehensive ambient noise data on the continent (Olugboji & Xue, 2022).

As a result, these models are limited in their resolution of Africa's crust in two key respects. First, because they do not include shortest period measurements, they lack sensitivity to absolute velocity in the shallowest crust (Roux et al., 2005; Yang et al., 2008). Second, because the continent-wide models do not include seismic data acquired in the past decade (2013–2023) (Accardo et al., 2017; Borrego et al., 2018; Celli, Lebedev, Schaeffer, & Gaina, 2020; Emry et al., 2019; Fadel et al., 2020; Wang et al., 2019; White-Gaynor et al., 2021), they lack spatial resolution across key tectonic domains. Here, we address this and other key issues necessary for building an updated model of Africa's crust using the ambient noise data set and model assessment product (ADAMA) provided by (Olugboji & Xue, 2022). We use these measurements to construct continent-wide Love and Rayleigh wave dispersion maps using a probabilistic approach. The inclusion of short-period surface wave measurements improves constraints on short-wavelength features (Lebedev et al., 2013). This allows us to provide greater resolution of the shallowest crust (Figures 1b and 2a).

In constructing new dispersion maps, we adopt a probabilistic Bayesian approach that solves for an image of surface wave speeds in the presence of irregular ray path coverage and variable measurement quality (Bodin et al., 2009; Bodin, Sambridge, Tkalčić, et al., 2012; Bodin & Sambridge, 2009; Bodin, Sambridge, Rawlinson, & Arroucau, 2012; Olugboji et al., 2017). This technique is well suited to the data set obtained from Africa. Furthermore, it also provides information on statistical significance—that is, error maps that quantify uncertainties in the final reported dispersion maps (Bodin, Sambridge, Tkalčić, et al., 2012; Olugboji et al., 2017). The dispersion maps with associated uncertainties are a useful data product since they span the entire continent and can be used to assess (Olugboji et al., 2017) and update existing models during linear and non-linear inversions for elastic properties in the crust (Shen et al., 2016; Shen & Ritzwoller, 2016).

In the rest of our paper we describe, in detail, the construction of our new maps, highlighting key benefits of adopting a probabilistic Bayesian approach. We show how the comprehensive ADAMA data set produces new illumination of crustal structure. We investigate the statistics and resolution present in the maps using the ensemble results obtained from sampling the posterior distribution. We then compare our results to existing published results at similar periods. We provide an assessment of one of the global velocity models, Litho1.0, by inverting the phase maps for depth dependent shear-wave velocity structure in Africa's crust. Finally, we generate a crustal taxonomy derived from unsupervised machine learning and discuss its implications for unanswered questions in Africa's crustal architecture: for example, secular evolution of the crust and its connection to tectonics and basement geology.

2. Continent-Wide Ambient Noise Data Set From ADAMA

The data set used in this study—ADAMA—is from the recently published catalog of continent-wide inter-station dispersion measurements provided by (Olugboji & Xue, 2022). This is a large catalog of Love and Rayleigh wave phase and group dispersion measurements. It represents the following advances: (a) it is a large distribution of short period dispersion measurements: ∼114,000 interstation pairs at periods between 5 and 40 s, (b) it includes uncertainties, and (c) is extracted from cross-spectra of continuous recordings of ambient noise ground vibrations, collected over four decades, since the commencement of digital seismometry on the continent. The inter-station cross-spectra are calculated from seismograms downloaded from

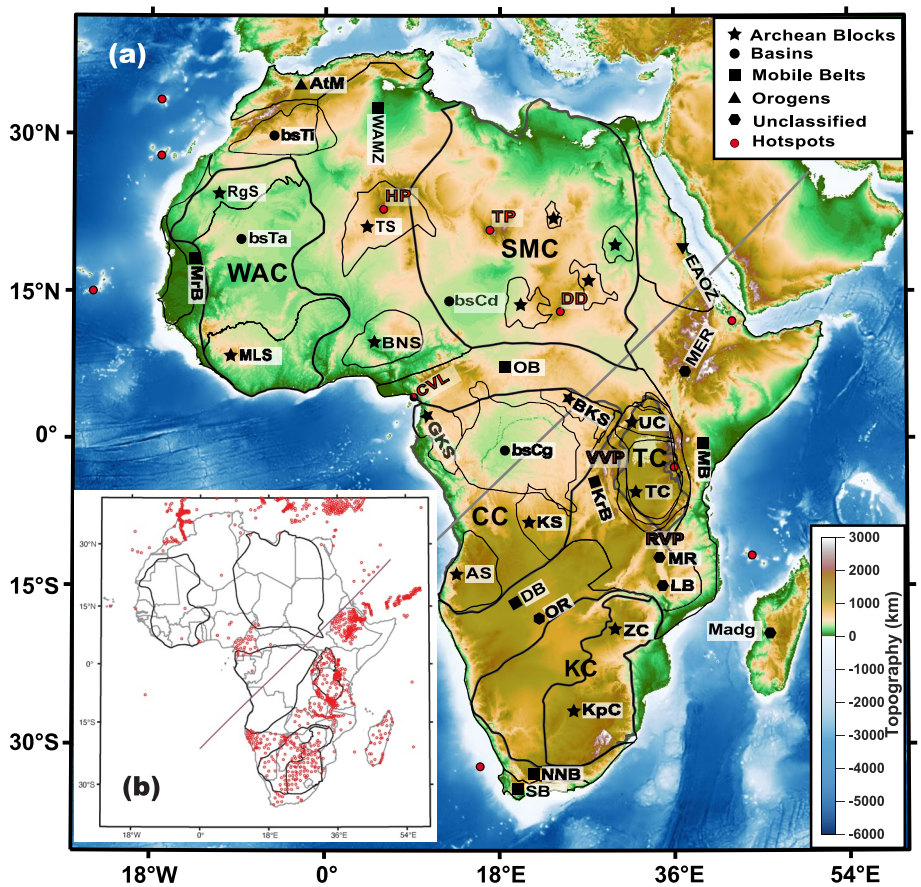

Figure 1. Africa's geology overlaid on topography (a) (Meta)-Cratons: WAC, SMC, TC, CC, KC: West Africa Craton, Sahara Metacraton, Tanzania Craton, Congo Craton, Kalahari Craton. Terranes in legend adapted from Begg et al. (2009): **I. Archean Blocks** (★): in **WAC**: MLS, RgS: Man-Leo Shield, Reguibat Shield; in **TC**, in **CC**: AS, BKS, GKS, KS: Angolan Shield, Bomu-Kibalan Shield, Gabon-Kamerun Shield, Kasai Shield; in **SMC**; in **WAMZ**: BNS, TS: Benin-Nigeria Shield, Tuareg Shield; in **KC**: ZC, KpC: Zimbabwe Craton, Kaapvaal Craton. **II. Basins** (●): **in CC**: bsCg: Congo Basin; **in AtM**: bsTi, bsTa: Tindouf and Taoudeni Basins. **III. Mobile Belts** (■): WAMZ, OB, DB, MB, NNB, KrB, SB: West Africa Mobile Zone, Oubangides Belt, Damara Belt, Mozambique Belt, Kibaran Belt, Namaqua-Natal Belt, Saldania Belt; **IV. Orogens** (▲): AtM, EAOZ: Atlas Mountains, East-Africa Orogenic Zone; **V. Unclassified** (⬟): **Madagascar** (Madg); **Other Cratons**: UC, ZC: Uganda Craton, Zimbabwe Craton; **Others**: AF, bsCd, LB, MER, MR, OR: Afar; Chad Basin; Lurio Block; Main Ethiopian Rift, Malawi Rift, Okavango Rift. **Hotspots** (●) : HP, TP, DD, VVP, RVP, CVL: Hoggar Plateau, Tibesti Plateau, Darfur Dome, Virunga Volcanic Province, Rungwe Volcanic Province, Cameroon Volcanic Line (b: Inset): Station distribution (red dots) used to obtain dispersion data set. East-west transect same as Figures 7 and 9.

1,372 stations, spanning 62 networks in and across Africa (e.g., southern Europe, and the Middle East). The inter-station ray paths provide improved spatial coverage and depth resolution across the entire continent (Figures 1b and 2a).

2.1. Love and Rayleigh Waves Dispersion With Uncertainties

For each station pair, phase and group velocities of Love and Rayleigh waves between 5 and 40 s are reported. Measurement uncertainty is also reported using a non-linear waveform fitting of the ambient noise cross-spectra, providing necessary regularization information during probabilistic inversion of our maps (Hawkins & Sambridge, 2019). For a detailed description of the data set catalog, we refer the reader to (Olugboji & Xue, 2022). Here, we describe how improved spatial coverage with short-period measurements extend the resolution of the crust. The catalog of inter-station dispersion measurements is used to obtain dispersion maps, uncertainties and shear-velocity in the entire crust.

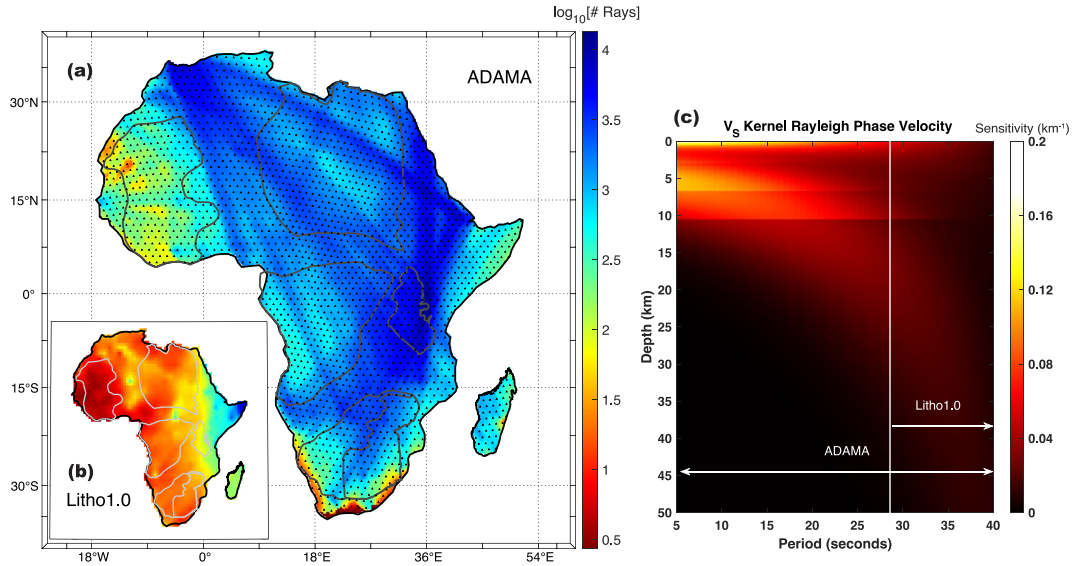

Figure 2. Shear wave sensitivity to Spatial coverage and Rayleigh wave for the ADAMA data set. (a, b) Raypath density for the ADAMA data set compared to a global model published in 2014 (Pasyanos et al., 2014). (c) Improved depth-sensitivity of ADAMA compared to the global Litho1.0 model showing improvements from short-period measurements.

2.2. Ray Coverage and Depth Sensitivity to Crustal Structure

The ADAMA data set improves on global and regional surface wave dispersion catalogs in two regards: the first is increased ray-path density with better spatial sampling across the entire continent and second is that it extends the surface wave dispersion measurements to very short periods (<25 s). At the shortest periods, and with rays sampling the entire continent, good resolution of the crust is possible (Figure 2). The latest data set encompasses measurements that are three orders of magnitude greater than the most recent continent-wide study (Emry et al., 2019).

3. Methods

3.1. Auto Adaptive and Probabilistic Noise Maps for Model Update of Africa's Crust

We construct dispersion maps with a probabilistic inverse approach. We solve for the spatial distribution of phase and group speeds, with associated uncertainties, while imposing minimal restrictions on parameterization and regularization. In Africa, where spatial sampling is highly irregular, and crustal structure is heterogeneous, an optimal parameterization along with modeling uncertainties can still be recovered during tomographic inversion. The technique is known as transdimensional hierarchical Bayesian inversion (THBI), and has been widely used by many authors to construct surface wave dispersion maps (see Crowder et al., 2019; Galetti et al., 2016; Pilia et al., 2020; Rawlinson et al., 2016; Zulfakriza et al., 2014). A comprehensive discussion of THBI can be found in Bodin et al. (2009), Bodin, Sambridge, Rawlinson, and Arroucau (2012), and Bodin, Sambridge, Tkalčić, et al. (2012). Here we provide a brief overview of the approach, show how we apply it to the ADAMA data set, and describe how we use the maps themselves for model assessment and update of the African crust (Olugboji et al., 2017). The new maps, constructed with THBI, contain information across multiple scales, with resolution not yet assimilated into the continent-wide models (Pasyanos et al., 2014; Sammon et al., 2022; Wipperfurth et al., 2020). We compare model predictions of dispersion with our new dispersion maps. Tests of statistical significance and an evaluation of improved resolution are estimated using ensemble statistics. In regions of improved spatial coverage, where model predictions are different from data (dispersion maps), updates to crustal structure are obtained. We report updates in these regions using a perturbational inverse approach (Haney & Tsai, 2017, 2020).

3.2. Noise Maps With Transdimensional Hierarchical Bayesian Inversion

The transdimensional and hierarchical Bayesian inverse approach is a class of sampling methods that seeks not just a single optimal model (dispersion maps), but rather searches the parameter space for all possible model

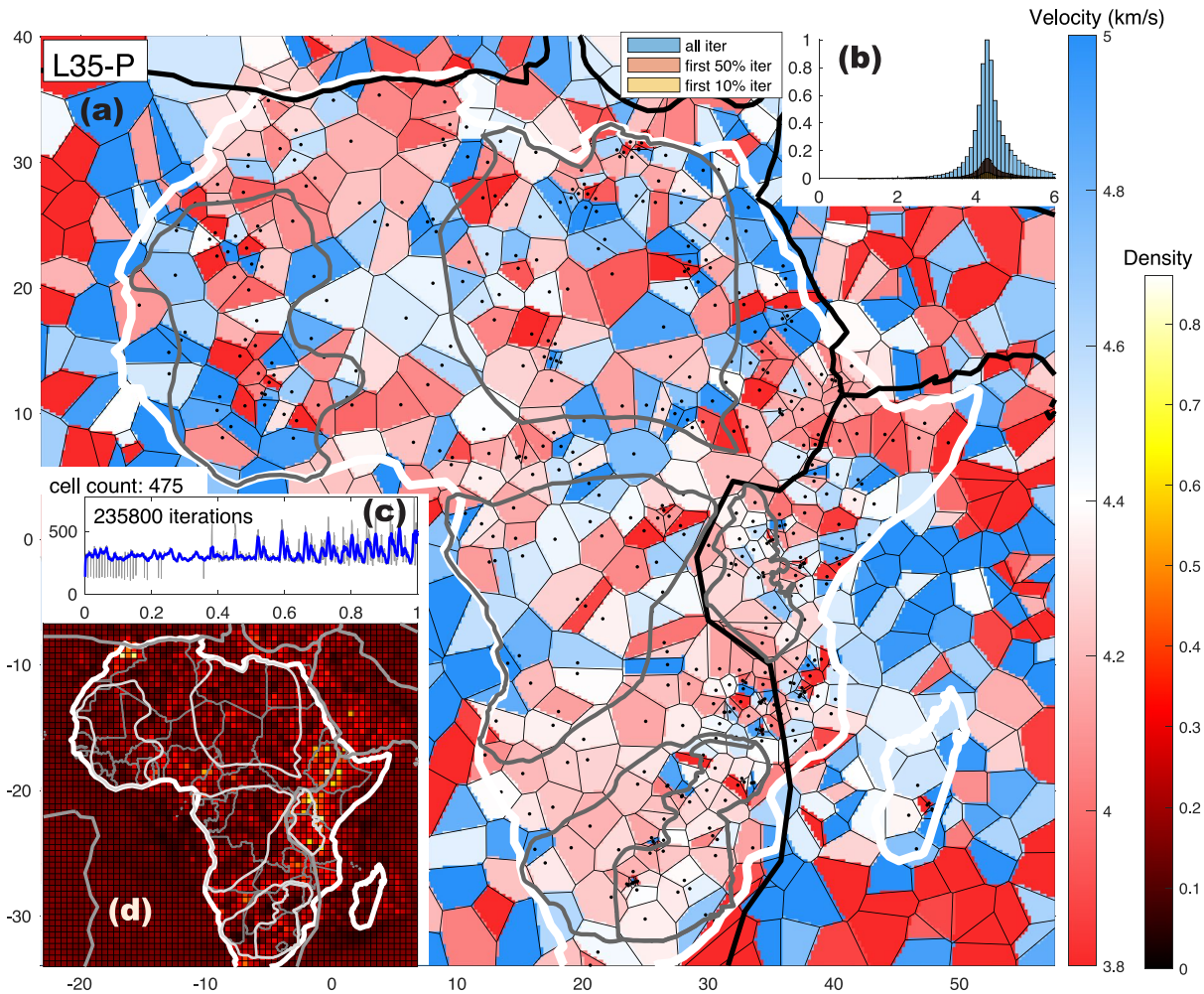

Figure 3. A snapshot through the Transdimensional Hierarchical Bayesian Inversion algorithm. (a) A single snapshot of model, **m**, showing the irregular Voronoi tessellation used to parameterize the Love wave 2-D phase velocity map at 35 s. The velocity values are constant within each cell and the node centers are irregularly located in the domain (black dots). (b) The posterior distribution of the phase velocity map (blue) and after discarding the first 10% or 50% of the samples (c) A time-series tracking the total number of Voronoi cells across all parallel chains in the Monte Carlo random walk. (d) A similar statistical analysis but showing the Voronoi cell density (number of cells per pixel) across all the chains.

solutions that best satisfy the observational constraints (interstation dispersion measurements). The ensemble of model solutions is then used to evaluate formal uncertainty. In this approach Bayesian statistics is applied to the twin challenges of model regularization and non-uniqueness. In the first step, transdimensional inference recognizes that the image reconstruction requires the parameterization of a 2-D surface velocity field, **V(r).** This is specified by a variable number of basis (descriptor) functions and values, which are unknowns to be solved:

$$\mathbf{V}(\mathbf{r}) = \sum_{i}^{N_i} \upsilon_i \mathbf{I_i} \tag{1}$$

Where the N_i velocity values, υ_i, sampled at points $\mathbf{r_i}$ are allowed to vary across the 2-D surface, thus ensuring that the velocity field is adaptively parametrized. In our implementation, we use a nearest-neighbor Voronoi tessellation (Figure 3a) as the basis function $\mathbf{I_i}$ (Sambridge et al., 1995). This function tessellates the velocity field, **V(r)**, and is widely used in transdimensional inversion (Bodin et al., 2009; Bodin, Sambridge, Rawlinson, & Arroucau, 2012). We note here that other forms of tessellations have recently been advocated (Belhadj et al., 2018; Hawkins et al., 2019) with beneficial properties like smoothness.

In the second step, the hierarchical inference recognizes that all inverse problems are fraught with uncertainty. That is, given the data vector of observations, d, and the model parameters $\mathbf{m} = \{v_i, r_i, N_i\}$ representing our 2-D image of the earth, errors are expected:

$$g(\mathbf{m}) = \mathbf{d} + \epsilon \tag{2}$$

The errors, $\epsilon = \epsilon_{data} + \epsilon_{theory} + \epsilon + \ldots$, can either be due to: (a) simplifying assumptions posed by our forward modeling operator $g(\mathbf{m})$ (e.g., in our case using ray theory (Shen & Ritzwoller, 2016) instead of eikonal tomography (Lin et al., 2009; Zhou et al., 2012)), (b) observational noise which cannot be modeled even in the case of a true model $g(\mathbf{m}_{\text{true}})$, or (c) sampling and discretization errors introduced from an approximate parameterization as described in Equation 1 above. In the Bayesian framework, the likelihood of a particular set of model predictions are those that minimize the probability on the prediction error term, and by definition maximizes the Gaussian likelihood:

$$p(\mathbf{d}|\mathbf{m}) = \frac{1}{\prod_j \sqrt{2\pi\sigma_j}} \exp\left(- \sum_j \frac{(g(\mathbf{m})_j - \mathbf{d}_j)^2}{2\sigma_j^2} \right) \tag{3}$$

The standard deviation term, σ, is the hierarchical parameter, and is an additional model parameter to be solved for with the hierarchical Bayes (Malinverno & Briggs, 2004) inversion. Note that it is defined in a way so as to represent all of the sources of error present in modeling and observation, so: $\sigma_i = \sigma_{i,data} + \sigma_{theory}$. Admittedly this is a rather simplistic model, since we do not investigate covariation in measurement errors. Nonetheless, by solving for a single scaling parameter for each period, we can accommodate for this, so that:

$$\sigma_i = \lambda \sigma_{i,data} \tag{4}$$

In summary, a transdimensional and hierarchical Bayesian inverse solution of our ambient noise dispersion measurements produces dispersion maps that involves sampling the posterior probability distribution for a collection of extended set of model parameters:

$$\mathbf{X} = \{\mathbf{m}, \lambda\} = \{v_i, r_i, N_i, \lambda\} \tag{5}$$

$$P\left(\mathbf{X}|\mathbf{d}_j = t_j^{c,u}\right) \propto P\left(\mathbf{d}_j = t_j^{c,u}|\mathbf{X}\right) p(\mathbf{X}) \tag{6}$$

Where $p(\mathbf{X})$ and $P\left(\mathbf{d_j} = t_j^{c,u}|\mathbf{X}\right)$ are the prior and likelihood on the extended set of model parameters $\mathbf{X}$ (actual model parameterization, $\mathbf{m}$, and hierarchical uncertainties λ), $\mathbf{d_j}$ is the data (dispersion measurements), N_j is the number of inter-station travel time measurements, for station separation, r_j, using either the interstation phase velocity, c_j or group velocity, u_j: $t_j^c = c_j/r_j; t_j^u = u_j/r_j$. The prior distribution is a uniform distribution, $p(\mathbf{X}) = \frac{1}{\beta - \alpha}$, on the set of model parameters, $\mathbf{X}$ (in Equation 5) and is specified by identifying the lower and upper limits (α, β). For a summary of the most relevant parameters in the THBI process see Table 1.

The solution to $\mathbf{X}$ is found by sampling the posterior distribution in Equation 6 using a reversible-jump Markov chain Monte Carlo (rj-McMC) algorithm (Green, 1995). The algorithm proceeds through a random walk by perturbing an initial model $\mathbf{X}$ to give $\mathbf{X}'$ on every step, adding $\mathbf{X}'$ to a collection of likely models and setting $\mathbf{X}'$ back to $\mathbf{X}$ if the model is accepted. Accepting (or rejecting) a proposed model is governed by acceptance probabilities that are defined in order to allow efficient sampling of the posterior distribution, and include models that, in the long run, increase the likelihood ratio of new proposed models. In this description, we leave the details of acceptance probabilities to the following papers for a complete discussion (Bodin et al., 2009; Hawkins et al., 2019). We point out that in the reversible jump transdimensional step, the number of model parameters, that is the set $\mathbf{m} = \{v_i, r_i, N_i\}$, is allowed to grow or shrink on every rjMcMC step. These steps are often referred to as the birth and death steps. They represent two of the four perturbation states when going from $\mathbf{X}$ to $\mathbf{X}'$ (Figures 3b–3d). The other two perturbation states involve changing the velocity values, v_i or the hierarchical noise parameter, λ. Therefore, given a collection of N_k steps, sampled over N_c parallel chains, we obtain a final average phase or group velocity map by using the entire ensemble $\mathbf{X}_k$ (Figure 4a):

$$\bar{V}^{p,g}(\omega_l, \mathbf{r}) = \int_m \mathbf{m} P(\mathbf{m}) d\mathbf{m} \approx \frac{1}{N_T} \sum_{k=b+\Delta_k}^{k=N_k \times N_c} v_{ik}^{p,g} \mathbf{I}_i(\mathbf{r}_{ik}) \tag{7}$$

Table 1
A List of Variables and Definitions Used in Describing the Transdimensional and Hierarchical Bayesian Inverse Formulation

	Variable	Description
I. Bayesian probabilistic framework		
1	$P(\mathbf{X}\|\mathbf{d}_j = t_j^{c,u})$	Posterior distribution on model parameters X, given data, d
2	$p(\mathbf{X})$	Prior distribution on model parameters X
3	$P(\mathbf{d_j} = t_j^{c,u}\|\mathbf{X})$	Likelihood of data, d, given model X
4	$t_j^{c,u}$	Inter-station travel time measurements
II. Transdimensional and hierarchical model definition		
5	$\mathbf{X_k} = \{\mathbf{m_k}, \lambda_k\}$	A set of $3N_i + 2$ parameters for every k_{th} McMC step
6	$\mathbf{m_k} = \{v_{ik}, r_{ik}, N_{ik}\}$	The transdimensional model parameters
7	$\mathbf{V}(\mathbf{r})$	The Voronoi tessellation for a 2-D velocity field
8	$\mathbf{I}$	Interpolating function that uses the Voronoi nodes
9	N_i	Number of Voronoi nodes
10	λ_k	Observational error for each map
11	v_{ik}^p	Phase velocities at N_i nodes
12	v_{ik}^g	Group velocities at N_i nodes
13	$\mathbf{r}_{ik} = (\theta_{ik}, \phi_{ik})$	Location (longitude, latitude) of the center Voronoi nodes
III. Forward problem and observational data		
14	$g(\mathbf{m})$	Forward problem predicts data given model X (great circle, bezier, fast marching, etc.)
15	N_j	number of available interstation phase dispersion measurements
16	$\mathbf{d}_j = t_j^{c,u}$	Data is N_j travel-time observations
17	c_j	Phase dispersion measurement for stations i, j
18	u_j	Group dispersion measurement for stations i, j
19	r_j	Interstation distance
IV. McMC sampling strategy		
20	N_c	Number of chains run in parallel
21	N_k	Number of Monte Carlo (McMC) steps per chain
22	b	No of burnin steps discarded before averaging
23	Δ_k	Length of thinning steps ensures decorrelation during averaging

Where the equation represents ensemble averaging using the nearest-neighbor tessellation of the Voronoi cells centered at longitude and latitude node coordinates $\mathbf{r}_{ik} = (\theta_{ik}, \phi_{ik})$. Whether a phase or group velocity node is implied: v_{ik}^p, v_{ik}^g, is dependent on which data set is used, $\mathbf{d_j} = t_j^{c,u}$ (see Equation 6). During ensemble averaging, we use a total of N_T samples, discarding b burnin steps, and downsampling each chain using a thinning parameter Δ_k:

$$N_T = N_c \times \left(\frac{N_k - b}{\Delta_k} \right) \tag{8}$$

We also use the ensemble and its average to compute statistical estimators of the dispersion maps' posterior distribution: that is standard deviation or second moments (skewness) (Figures 4b and 4c), providing a quantitative measure of statistical significance (Bodin et al., 2009; Bodin & Sambridge, 2009; Bodin, Sambridge, Rawlinson, & Arroucau, 2012; Olugboji et al., 2017):

$$\xi^{p,g}(\omega_l, \mathbf{r}) = \int_m (\mathbf{m} - \bar{\mathbf{m}})^2 P(\mathbf{m}) d\mathbf{m} \approx \frac{1}{\sqrt{N_T}} \sum_{k=b+\Delta_k}^{k=N_k \times N_c} \left[v_{ik}^{p,g} \mathbf{I}_i(\mathbf{r}_{ik}) - \bar{V}^{p,g} \right]^2 \tag{9}$$

In one sense, the average dispersion maps are solutions of an inverse transformation g^{-1} obtained through Monte Carlo Markov chain (McMC) sampling. The McMC sampling transforms the inter-station travel-time

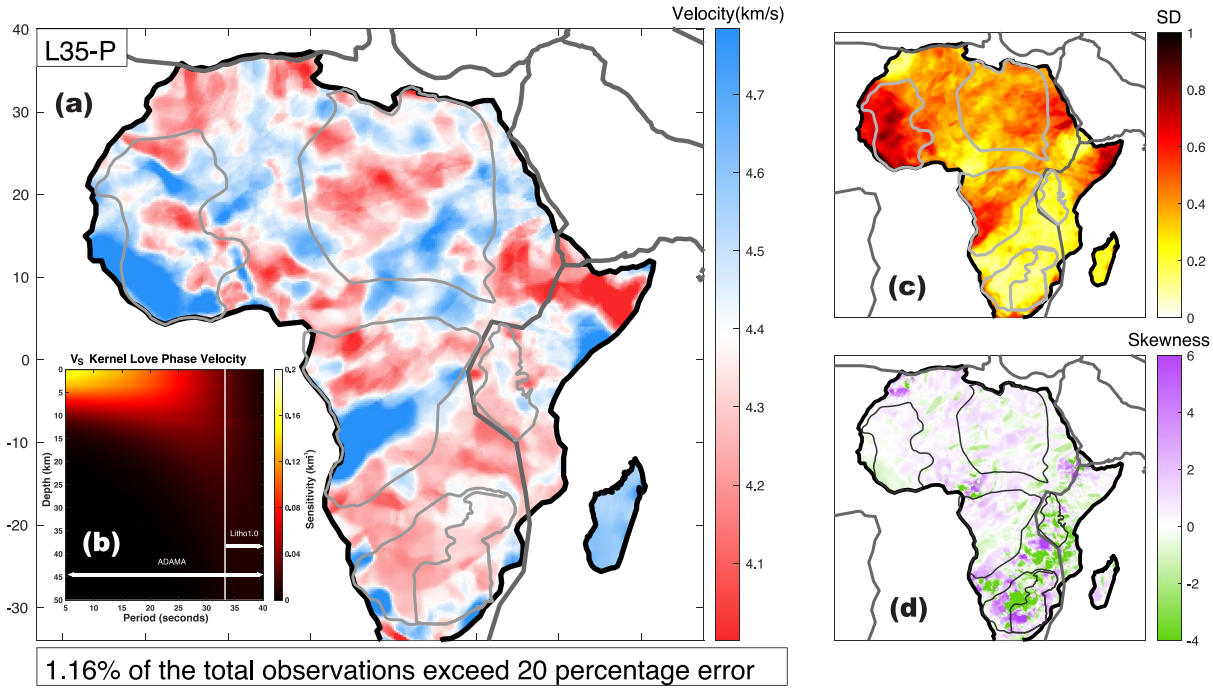

Figure 4. Statistical estimators of the posterior distribution on the 30 s-Love wave phase map. (a) The mean dispersion map. (b) The sensitivity of Love waves to shear-wave velocity. (c) The standard deviation of the phase map provides an estimate of uncertainty in the phase map shown in (a) as reconstructed during the sampling of the posterior distribution. (d) A second estimator of the statistics of the posterior distribution, the skewness (second-moment) of the probability distribution showing deviation from non-Gaussian statistics.

observations, N_j data vectors, into N_R dispersion curves: $\left[\mathbf{d_j} = t\right] \overset{g^{-1} \approx P(\mathbf{X})}{\rightarrow} [\mathbf{d_R} = V^{p,g}]$. The dispersion curve at each point on the African continent can then be used to solve for an earth model, $\mathbf{m}^{\beta,\alpha,\rho}(z)$:

$$\mathbf{f}\left(\mathbf{m}^{\beta,\alpha,\rho}(z)\right) = \mathbf{d_R} \tag{10}$$

Where, $\mathbf{f}$ is a non-linear forward model that maps a local 1D earth model into our data of dispersion curves $\mathbf{d_R}$ and α, β are the compressional and shear velocities and ρ is the density, all varying with depth, z. We discuss, next, our approach to obtaining this earth model.

3.3. Shear-Velocity Model Assessment and Update Using a Perturbation Method

We use a perturbational approach to invert the Rayleigh wave phase velocity maps for an updated earth model (Haney & Tsai, 2017). The shear velocity model of the global lithospheric model of Pasyanos et al. (2014) is used as a starting model. The perturbational approach uses an iterative gradient descent method to solve the nonlinear inverse problem (Equation 10) using a modified augmented system of equations:

$$\begin{bmatrix} \mathbf{C_d^{-1/2}G} \\ \mathbf{C_m^{-1/2}I} \end{bmatrix} \mathbf{\Delta m_k^{\beta}} = \begin{bmatrix} \mathbf{C_d^{-1/2}\Delta d_k} \\ \mathbf{0} \end{bmatrix} \tag{11a}$$

$$\mathbf{F_k \Delta m_k^{\beta}} = \mathbf{D_k} \tag{11b}$$

b.1: Iterative solution starts with: $\mathbf{m_0^{\beta}} : \mathbf{\Delta d_k} = \mathbf{d_R} - \mathbf{f}\left(\mathbf{m_k^{\beta}}\right)$
b.2: Solving: $\mathbf{\Delta m_k^{\beta}} = \left[\mathbf{F_k^T F_k}\right]^{-1} \mathbf{F_k^T D_k}$
b.3: Updating: $\mathbf{m_{k+1}^{\beta}} = \mathbf{m_k^{\beta}} + \mathbf{\Delta m_k^{\beta}}$
b.4: Repeating until: $\chi^2 \approx \frac{\mathbf{D_k^T D_k}}{F} \leq 1 + \epsilon$

Where $\mathbf{m}_0^\beta$ and $\mathbf{\Delta m}_\mathbf{k}^\beta$ are the shear wave velocity and its kth update and $\mathbf{d_R}$ and $\mathbf{\Delta d_k}$ are the observed dispersion curves and the prediction error for each iteration (Equation 10). The stopping criterion is reached (Equation 11b.4) when the dispersion measurements are matched by the predicted data for a given number of measurements, $F = l$ and $\epsilon = 0.5$. The augmented system (Equation 11a) requires computing the sensitivity kernel $\mathbf{G}$, and the data and model covariance matrices, $\mathbf{C_d}$ and $\mathbf{C_m}$:

$$\mathbf{C_d} = \xi^2(\omega)\mathbf{I} \tag{12a}$$

$$\mathbf{C_m} = \gamma\xi^2(\omega)\exp\left(\frac{-|z_i - z_j|}{d}\right) \tag{12b}$$

Data covariance is diagonal and prescribed from measurement uncertainties obtained from Bayesian inversion (Equation 9), while the full matrix representing the covariance of model parameters at depth nodes z_i and z_j is prescribed by two user-supplied factors: a smoothing distance or correlation length, d, and a scaling factor γ. These parameters prescribe some type of regularization to the model solution and weight the degree of data fit.

In model assessment, we constrain shear-wave velocity by assuming (a) that the Poisson ratio and densities of the Litho1.0 model are fixed or (b) compressional velocity and density can be estimated from shear velocity, using scaling relationships derived from empirical measurements of rock elasticities (Brocher, 2005). We then construct an updated model of Africa's Crust Evaluated with ADAMA Rayleigh Phase maps (ACE-ADAMA-RP) following the iterative scheme of Equation 11. We point out that this is just one way to use the new ADAMA data set. In principle, we could construct a model not tied to any starting reference model. Alternatively, we could use all the surface wave dispersion maps—Love and Rayleigh including group velocity as well as phase velocities (ACE-ADAMA-SW). Additionally, we could adopt a similar probabilistic approach to jointly invert the surface wave dispersion data sets with other body-wave seismic measurements like receiver functions (Bodin, Sambridge, Tkalčić, et al., 2012). We defer this to future work. Here, we focus on producing a model update (ACE-ADAMA-RP) based on a reference global model (Litho1.0). This provides a quick benchmark of our new dispersion maps. The updated model can then be evaluated in the context of statistics derived from the computationally expensive THBI algorithm.

4. Results

We summarize the THBI solutions using representative Rayleigh and Love wave phase dispersion maps discretely sampled at four periods (8, 15, 20, and 35). The full solution is archived as a digital open source model (see data acknowledgment) and represents a finer sampling at $l = 11$ periods. The maps include Love and Rayleigh phase and group dispersion maps at each of the 11 discretely sampled periods for a total of 44 maps $2 \times 2 \times 11 = 44$. A summary of the ensemble statistics is provided in Tables 2 and 3. The posterior distribution for the entire set of dispersion maps, providing insights into which regions in Africa are best resolved; that is, which regions are constrained with high precision and are not biased toward unreasonably large or small velocities. Finally, we present illustrative examples of the new model of Africa's crustal shear-velocity model (ACE-ADAMA-RP).

4.1. THBI Solutions: Exemplary Phase Maps With Errors

The rj-McMC algorithm is run on ~20 parallel chains for a total of 1 million iterations. For each Markov chain, accepted model ensembles are downsampled every 100 steps. The final averages and standard deviations are computed to produce final Love and Rayleigh wave dispersion maps. We downsample, or "thin," the ensemble to avoid potential biases from interdependence (Bodin et al., 2009; Olugboji et al., 2017). We show exemplary maps at four distinct periods, from the shortest to longest periods (Figures 5 and 6). Dispersion maps display spatial heterogeneity that depends on wavelength: more heterogeneity at shorter periods compared to the longest periods.

At the shortest periods (<12 s) we observe faster velocities in west and central Africa than in east and southern Africa (Figures 5a1–5d1). Similar patterns of heterogeneity are observed for Love as well as Rayleigh dispersion. Love waves travel faster than Rayleigh waves and are therefore more sensitive to shallow crustal structure (compare Figure 4b to Figure 2c). This explains why, at the shortest periods, the Love wave maps are more heterogeneous than the corresponding Rayleigh maps (compare Figures 5b1 and 6b1 and Figures 5b2 and 6b2).

Geochemistry, Geophysics, Geosystems

10.1029/2023GC011086

Table 2
Phase Velocities

Prior distributions								
Min cell (200) Max cell (2000) initial cell (320) Min group sigma (1) Max group sigma (45)								
	Rayleigh				Love			
	σ_i		$\overline{C}^R$		σ_i		$\overline{C}^L$	
T	MIN	MAX	MIN	MAX	MIN	MAX	MIN	MAX
5	12	45	0.2	6	12	45	0.2	6
6	1	45	0.2	5.5	1	45	0.2	6
8	1	45	0.2	6	1	45	0.2	6
10	1	25	0.5	6	10	45	0.2	5.5
12	1	40	0.2	6	1	40	0.2	6
15	1	40	1	6	1	40	1	6
20	1	40	0.5	6	1	40	0.5	6
25	1	30	0.5	6	1	30	0.5	6
30	1	30	0.5	6	1	30	0.5	6
35	1	25	1	6	1	25	1	6
40	1	20	1.5	6.5	1	20	1	6.5

	Posterior distributions			
	Rayleigh		Love	
T	$\overline{N}_i$	$\overline{C}^R$	$\overline{N}_i$	$\overline{C}^L$
5	582	3.73	248[a]	3.92[a]
6	437	3.63	258	3.98
8	452	3.74	331	3.99
10	310	3.75	216	3.93
12	327	3.73	286	4.05
15	433	3.73	393	4.11
20	401	3.81	673	4.16
25	403	3.91	359[a]	4.21[a]
30	374	4.00	468	4.30
35	321	4.05	322	4.36
40	334	4.14	388	4.44

[a]Not fully converged.

Table 3
Group Velocities

Prior distributions					Posterior distributions			
	Rayleigh		Love		Rayleigh		Love	
	U_i		U_i		$\bar{N}_i$	U_i	$\bar{N}_i$	U_i
T	MIN	MAX	MIN	MAX	–	–	–	–
5	0.2	5.5	0.2	5.5	306	3.61	308	3.66
6	0.2	5.5	0.2	6	284	3.64	431	3.83
8	0.2	5.8	0.2	6	361	3.69	374	3.86
10	0.5	6	0.2	6	776	3.68	400	3.86
12	0.5	6.2	0.5	6.2	358	3.70	279	3.92
15	1	6.5	0.5	6.5	540	3.68	334	3.97
20	1.5	6.5	1.5	7	600	3.54	571	3.98
25	1.5	7	1.5	7	690	3.61	703	3.99
30	2	7	1.5	7	389	3.72	711	4.07
35	2	7.5	2	7.5	434	3.86	414	4.17
40	2	7.5	2	8	455	3.94	618	4.29

In general, the error maps show that the standard deviations are lowest at the longest periods (long wavelength image >20 s) and when data coverage is the highest (south east vs. west and central Africa). This pattern in the error maps is replicated with our synthetic tests (Figure S1 in Supporting Information S1). We observe that the uncertainties are highest for checkerboard models and when data coverage is poor. In comparison, the long-wavelength toy models are better resolved especially in regions with good data coverage. These synthetic experiment suggest that the THBI algorithm can appropriately model uncertainties inherent in the measurement errors as well as those inherent in the reconstruction process. Although the synthetic tests show that the greatest uncertainties should be expected where the station coverage is sparse, statistically significant patterns are discernible even for regions with poor data coverage. For example, along the Congo craton where sampling is relatively sparse, stable high-velocity feautures can be resolved (compares Figures 5 and 6 with Figure 2a). We use the full statistics of the posterior distributions to explore these features. In particular, we describe which regions of our maps are resolved with high-precision and which are not. This is important for evaluating final updates to the crustal models.

4.2. Ensemble Statistics of Noise Maps: Convergence and Posterior Distributions

As we've pointed out, the spatial distribution of the standard-deviation (error maps) is fundamentally governed by measurement error and raypath sampling. As a result, we observe that the Rayleigh maps are better resolved than the Love maps. The noisiest maps are observed at the shortest periods. This is not surprising since horizontally polarized waves are noisier at these periods. We also observe that the most problematic maps are the 6 and 10 s maps (see also Table 1 of Olugboji and Xue (2022)). We determine precision by classifying each pixel based on: (a) its standard deviations and (b) the amplitude of the absolute velocity relative to a 1-D reference model (ak135). At each location, the dispersion maps are either precise or biased depending on these two measures. For example, a phase dispersion curve is highly precise and recovered with low bias when no more than two discrete periods have standard deviations that exceed 0.4 km/s with values that are not biased toward unreasonably high numbers (>40% of the reference value). Based on this scheme, we classify Africa into four categories: (a) High precision, (b) Low precision, (c) Biased, and (d) Unbiased regions based on the error statistics (Figure 7). This is a concise way to summarize the uncertainty inherent in our THBI dispersion maps. The statistics derived here are propagated onwards into the model update of Africa's crust.

We observe only a slight difference in Rayleigh and Love precision and bias: 64.4%, by area, for Rayleigh and 63.3%, by area, for Love. In particular, regions like Madagascar, the Sahara metacraton, the cratons of southern, central, and eastern Africa and the atlas mountains of North Africa are recovered with high precision and low bias (green dots of Figures 7a and 7b). While these regions are recovered with a high precision, some portions are highly biased. For example, the west-end of the Congo craton and the eastern edge of the Sahara meta-craton. Within this large sea of "high precision-low-bias" regions are regions on the east with low-precision-low-bias: the Horn of Africa and the western African craton (blue dots of Figures 7a and 7b). The western African craton also has the most regions with very highly biased dispersion curves (red dots of Figure 7). Again, these broad patterns are well explained by the raypath coverage. Regions with the lowest precision and that are highly biased often intersect with regions of very low ray path coverage—for example, the western Africa craton, the Horn of Africa, and the eastern edge of the Congo craton (see Figure 2a).

Compared to the phase dispersion maps, the group dispersion maps have larger uncertainties, with only 25.3% and 13.5% by area of Rayleigh, and Love, being recovered with high precision. Large portions have very low precision and high bias (Figures 7c and 7d). This makes it difficult to use the group dispersion results for continent-wide model assessment or update. Regardless, we observe improvements in precision at some specific regions, made possible by short-aperture, country-wide seismic array deployments. For example, in Morocco,

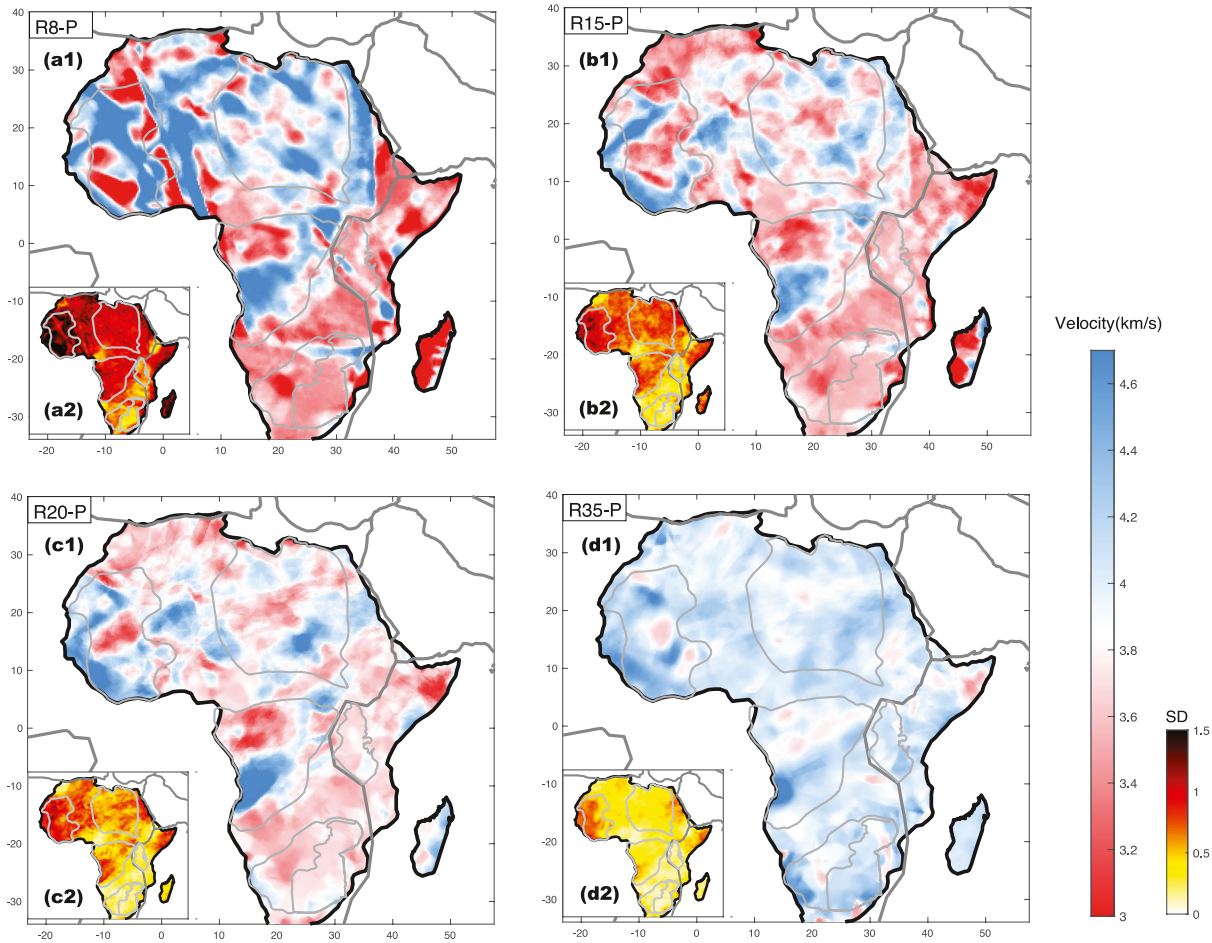

Figure 5. Rayleigh-wave phase maps and associated uncertainties at four discrete periods constructed using transdimensional hierarchical Bayesian inversion. (a1, b1, c1, d1) Average maps constructed using the posterior distributions. (a2, b2, c2, d2) The standard deviation maps constructed using a method similar to Figure 4c. For Rayleigh wave group velocity maps see Figure S2 in Supporting Information S1.

Cameroon, Ethiopia, Tanzania, and Southern Africa (Olugboji & Xue, 2022). Similarly, the cratons in the east and south of Africa are the best resolved as well as the highlands of Ethiopia, Morocco and the volcanic regions of Cameroon (compare Figures 7c and 7d with Figure 1b). Next, the group dispersion maps for Congo craton and Sahara metacraton are moderately well resolved. Along these cratons, only a few regions are highly biased with low-precision (i.e., the western edge of the Congo craton, and a few regions in the Sahara meta craton). Finally, we observe the worst resolution across the west African craton and along the mobile belts between the west African and sahara metacraton. In our current study, we do not use the group dispersion maps to inform the model update. However, other authors may elect to use it as a constraint for investigating targeted regional crustal structure especially in highly resolved regions. For completeness, we report the entire data set and provide the digital maps for reference. In general, the statistics of our dispersion maps shows that continent-wide model updates, using Rayleigh wave phase dispersion, are statistically significant there is room for improvement in low-resolution regions and we anticipate this will be possible with improvements in instrumentation (blue and red dots of Figure 7a).

4.3. Africa's Crustal Structure: Model Update and Assessment of Shear-Wave Velocity

To complete our analysis, we present a new continent-wide, shear-wave velocity model of the entire African continent. This model is based on the Rayleigh wave phase dispersion maps and uncertainties. The decision to use this dispersion data set is informed by the error statistics presented in the previous section (Figure 7). An attempt to use both phase and group dispersion would lead to a final crustal model that inherits a larger set of

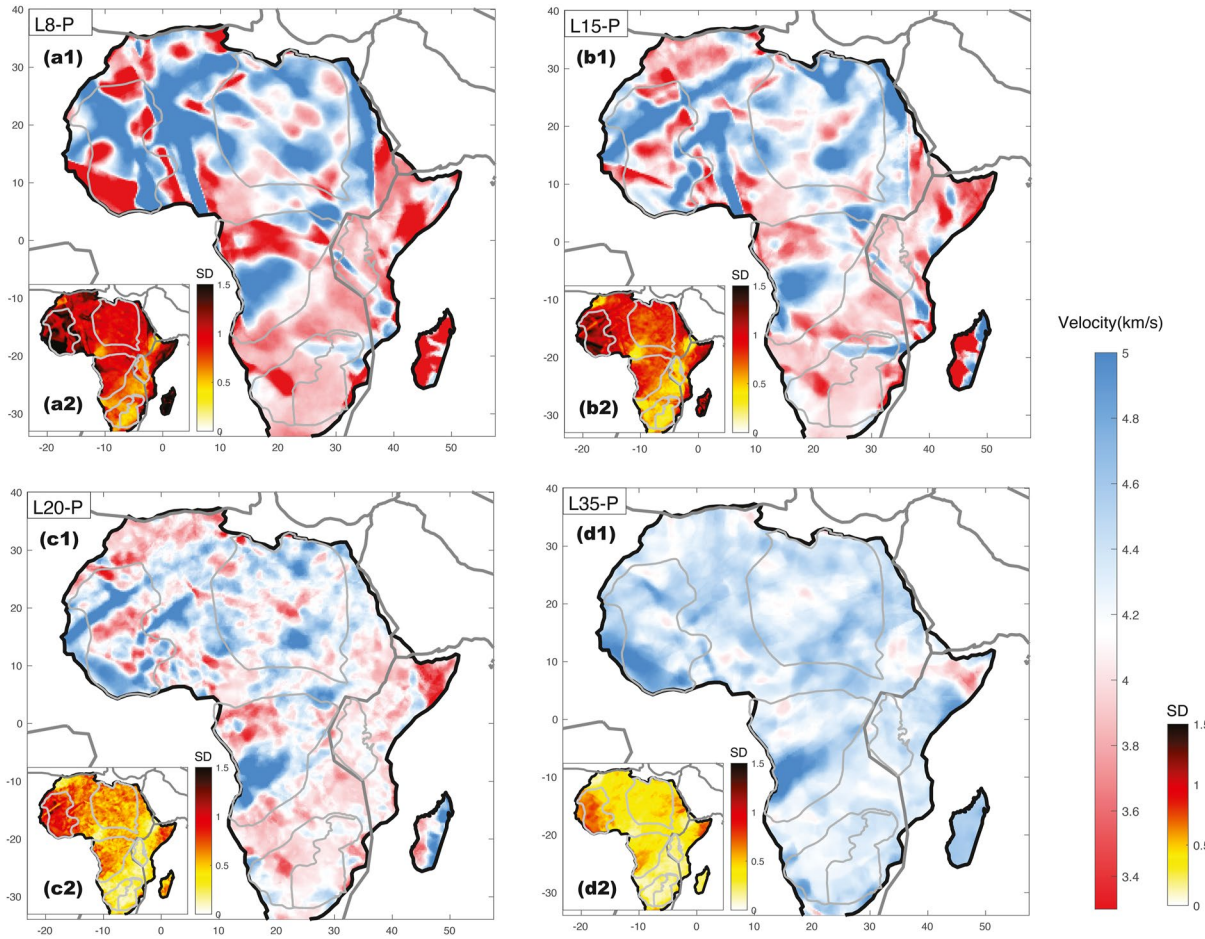

Figure 6. Same as Figure 5 but for Love-wave phase dispersion. For group velocity maps see Figure S3 in Supporting Information S1. For summaries of all maps at other periods see Tables 2 and 3.

biased and unreliable dispersion curves (Figures 7c and 7d). The new model is constructed using the Litho1.0 model as a reference starting model. Therefore, we consider it both a model update as well as a model assessment of the crust within Africa. An inversion at each grid point produces an updated 1-D model (Figure 8). We then interpolate these models into a quasi-3D shear velocity model. We visualize the final model by taking 2-D vertical and horizontal projections at selected transects and depth-slices across the entire model domain. A few such examples are selected to highlight geographic regions and crustal depths where we expect to see improvements in resolution (Figure 2b). The 2-D projections include: (a) a vertical slice defined by a transect that runs from the western edge of the Congo craton on toward Ethiopia (Figures 7a and 9) and (b) four horizontal slices spaced at 10-km intervals starting at the topmost crust and terminating around the Moho which is at 40 km for most of Africa (Figure 10).

The vertical slice through our updated crustal model illustrates the utility of ensemble statistics. The shear-velocities are typically left unchanged when ADAMA's Rayleigh dispersion curves do not statistically differ significantly from that of the starting reference model. Significant model updates are observed within the topmost crust (Figure 9a) informed by improved resolution at the shortest periods (Figure 2c). The updated crustal velocity model also includes uncertainties that have been forward propagated from the McMC ensemble (Figure S5b in Supporting Information S1). This shows that not all regions of our model update are equally well resolved. For example, along transect X′X, the shallow crust underneath the Angolan and Bomu-Kibalan shields are the least resolved with higher standard deviations and highly biased velocities (compare Figure 7a and Figure S5b in Supporting Information S1). This point is further elaborated by comparing the model updates, ACE-ADAMA-RP, with the Litho1.0 starting reference model (Figure 10 and Figure S6 in Supporting Information S1). We observe the largest differences within the top and middle crust (<20 km) especially along craton

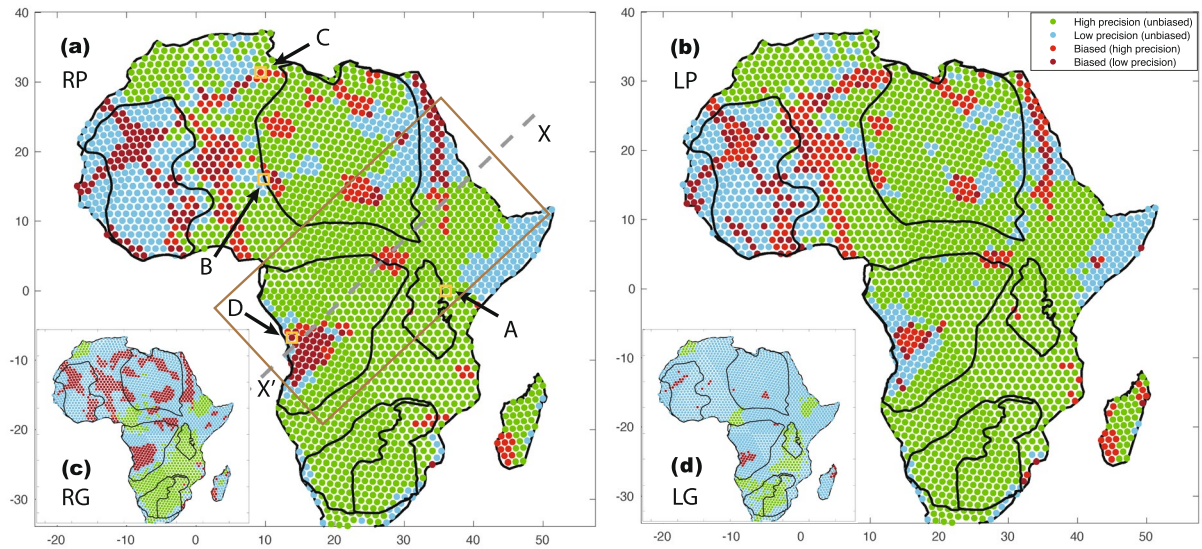

Figure 7. The quality of Rayleigh and Love dispersion models derived based on ensemble statistics. (a) The spatial statistics of Rayleigh phase dispersion is color-coded by precision and bias: high precision and unbiased (green), low precision and unbiased (blue) high-precision and biased (red), low precision and biased (brown). We identify four locations (A-B-C-D) that exemplify these four classes. (b) The spatial statistics of Love phase dispersion. (c) The spatial statistics of Rayleigh group dispersion. (d) The spatial statistics of Love group dispersion. Model update and assessment using Rayleigh phase dispersion curves and associated uncertainties are shown at the four locations (Figure 8) and on a transect **X′X** crossing south-west to north-east (Figure 9).

edges. The new model tends to have higher shear velocities compared to Litho1.0. Within the interiors of the Congo Craton and the Sahara Meta Craton new features are recovered that are absent in Litho1.0. For example, the high-velocity domains in the western edge of the Congo craton and within the North and eastern end of the Sahara Meta Craton (Figures 10a–10c).

While some of these features are recovered from the least resolved dispersion curves (high-velocity western boundaries of the western African and Congo craton), they cannot be entirely explained by poor measurements. This is because are spatially coherent across the entire crust and can be seen at the longest periods in both the Rayleigh and Love dispersion measurements, which are recovered with better resolution (compare e.g., Figure 7 with Figures 4–6). The spatial extent and the reliability of these features may require further tests as improvements in station coverage and data quality lead to improvements in spatial resolution and lead to more precise dispersion maps.

5. Discussion and Interpretation

We have constructed a continent-wide shear velocity model of the entire African continent and Madagascar using a probabilistic and perturbational inversion of the most comprehensive ambient noise dispersion measurements to date (Olugboji & Xue, 2022). This work, in Africa, is similar to other continent-wide studies that construct models of the crust based on short period passive source ambient noise seismic data (Lu et al., 2018; Saygin & Kennett, 2012; Shen et al., 2012). However, we have used the probabilistic approach to produce ambient noise dispersion maps (Eshetu et al., 2021; Galetti et al., 2016; Yuan & Bodin, 2018; Zulfakriza et al., 2014). The probabilistic approach has allowed us to pose, and answer, fundamental questions about the statistical significance of our new dispersion results. For example, we explore how new measurements inform model updates of Africa's crust (Olugboji et al., 2017): (a) at which periods are the dispersion maps best resolved? (b) which regions of Africa need significant updates, and which do not? (c) In the regions with improved resolution, and requiring significant model updates, to what degree do existing reference models differ from current model updates? Our current update of Africa's Crust (ACE-ADAMA-RP) answers all these questions. It extends our understanding of Africa's crustal architecture.

We reiterate that the model we have constructed here is derived from the vertically polarized ambient noise dispersion maps alone. Future work will explore other passive source data sets like receiver functions, earthquake surface wave tomography, and other seismic observables that extend resolution in the lithosphere from the crust into the upper mantle (Gao et al., 2022; Han et al., 2022; Shen et al., 2012, 2018). We anticipate that such efforts will extend lateral resolution only when data are collected in regions with poor spatial resolution, for example,

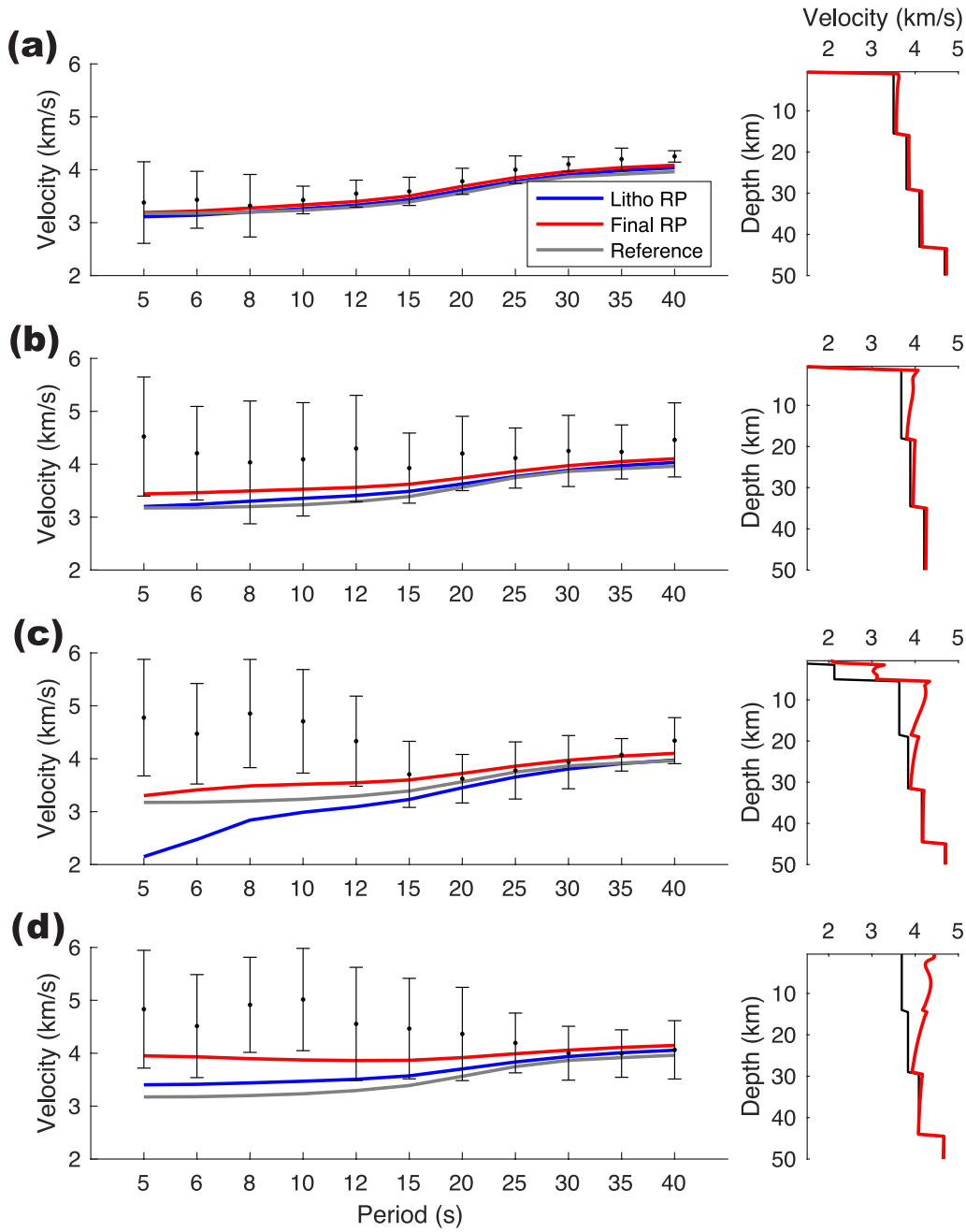

Figure 8. Illustrative examples showing model assessment and update of Litho1.0's shear-wave velocity using ADAMA's Rayleigh wave phase dispersion curve and uncertainties. Model assessment and update for: (a) a high precision and unbiased dispersion curve, starting phase velocity from Litho1.0 model (blue curve), final dispersion curve after the perturbational inversion scheme described in Section 3.3 (red line) (b) a low precision and unbiased dispersion data (c) a biased and low precision data (d) a biased and high precision data. The locations of the examples in (a)–(d) above are shown in Figure 7 (indicated by arrows). See Figure S4 in Supporting Information S1 for a more conservative inversion.

across the western Africa craton (Figure 7). When other passive source data sets are jointly interpreted, the improved depth resolution of other elastic-properties like compressional wave speed, Poisson ratio, is possible only when the measurements are made in regions with low-resolution. In what follows, we review the current state of seismic models of the African crust (Begg et al., 2009; Crosby et al., 2010; Finger et al., 2022; Raveloson et al., 2015). We contrast this with Moho models based on joint inversion with other geophysical methods to

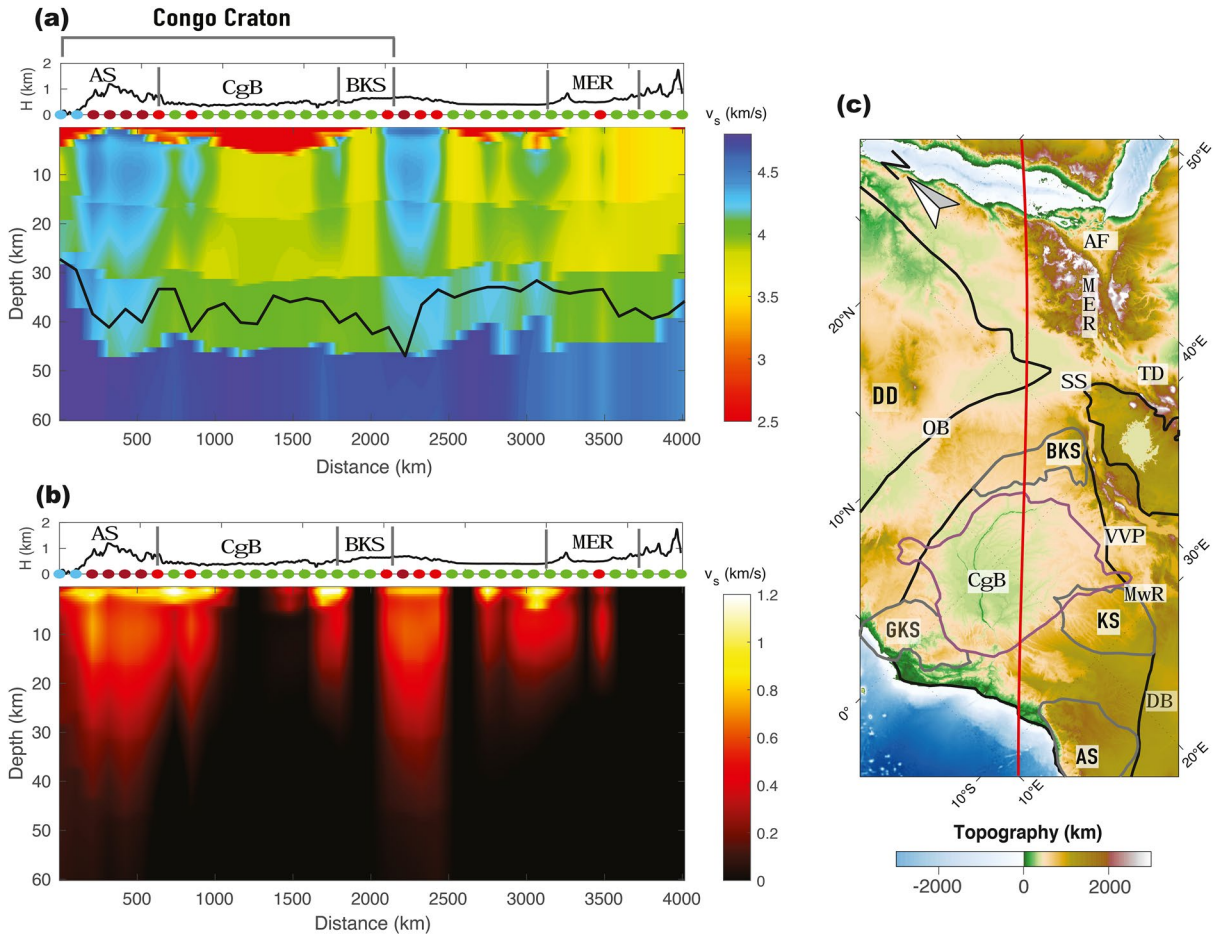

Figure 9. A vertical slice through, ACE-ADAMA-RP, the updated shear-velocity model of Africa's crust based on ADAMA's Rayleigh wave phase dispersion curves. (a) The shear velocity model through transect **X′X** starts from the western edge of the Congo craton on toward Ethiopia (see Figure 7a). The depth to the crust-mantle boundary is shown for reference and taken from Globig et al. (2016). (b) The difference between the final model and the starting model. (Top of 9a & 9b) Topography running through transect **X′X** with abbreviations same as in Figure 1a and statistical properties of each region (colored circles) same as in Figure 7a. (c) The geology surrounding transect **X′X** showing domains within the Congo craton, continental shield domains, the congo basin, and surrounding areas. The outline of the Congo basin is taken from Raveloson et al. (2015, 2021). For a view of the starting model used for the update and standard deviation of the final shear-velocity model see Figures S5a and S6 in Supporting Information S1.

obtain thermo-compositional models of the African lithosphere (Afonso et al., 2022; Globig et al., 2016; Haas et al., 2021; Raveloson et al., 2021).

5.1. Comparing ADAMA to Other Ambient Noise Models of Africa's Crust

A few previous studies have used ambient noise measurements to construct regional and continent-wide seismic velocity models on the continent (Accardo et al., 2017; Borrego et al., 2018; Emry et al., 2019; Fadel et al., 2020; S. Kim et al., 2012; Pasyanos et al., 2014; White-Gaynor et al., 2021; Yang et al., 2008). Only two of these extend across the continent and provide complete imaging of the African crust (Emry et al., 2019; Pasyanos et al., 2014). Both studies use fewer stations and calculate dispersion measurements at periods >30 s, therefore limiting their spatial resolution to long-wavelength features and their depth resolution to the lowermost crust and sub-Moho depths (>33 km). By comparison, our work extends the resolution of crustal structure both laterally and at depth, using a large catalog of shortest periods: 5–40 s (Figure 2b) (Olugboji & Xue, 2022). Other regional models (Borrego et al., 2018; Chambers et al., 2019; Eshetu et al., 2021; Fadel et al., 2020; S. Kim et al., 2012; Malory et al., 2022; Wang et al., 2019; White-Gaynor et al., 2021) do a similar job at providing improved depth and spatial resolution,

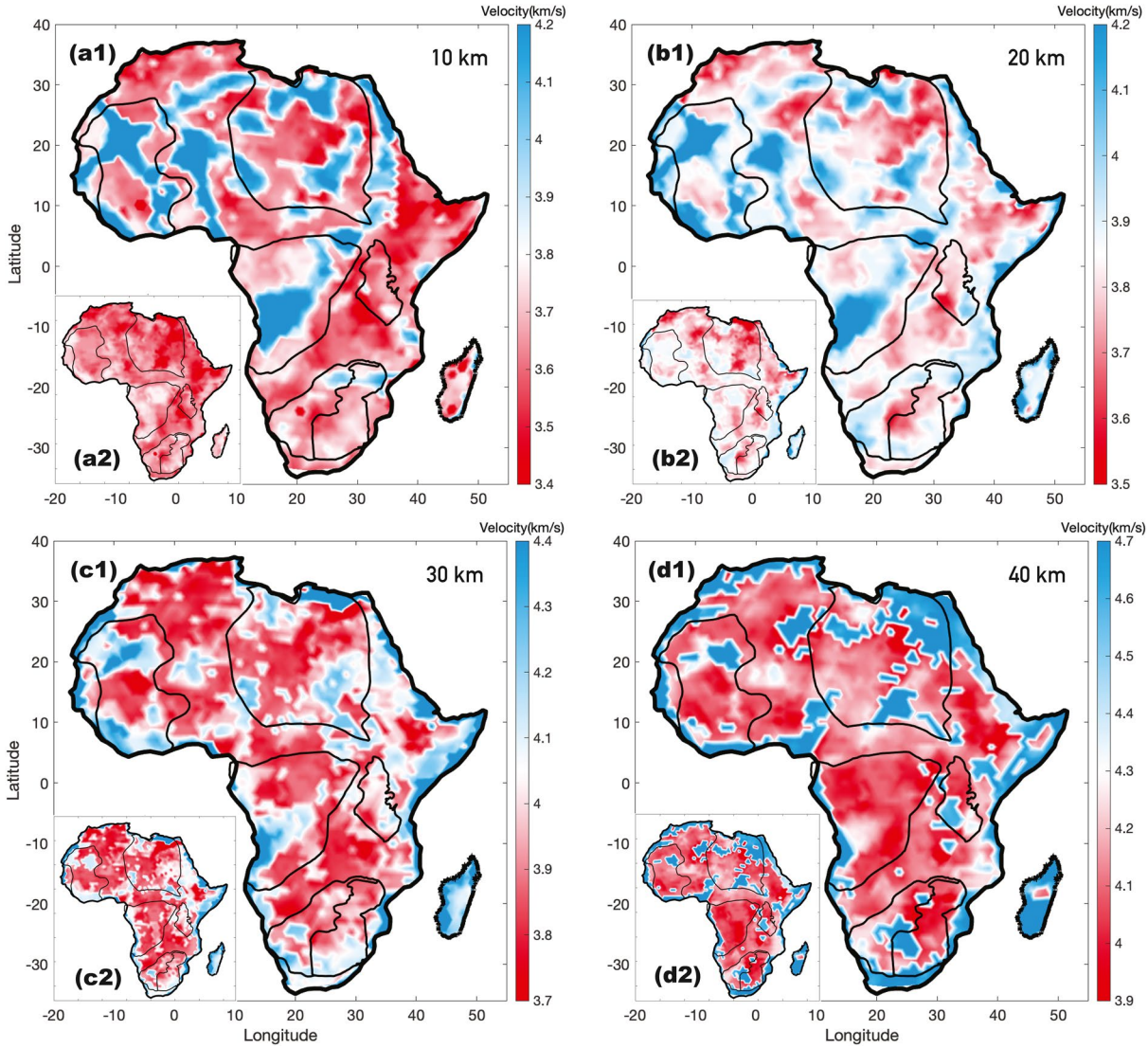

Figure 10. Horizontal slices through the updated shear-velocity model of Africa's crust. Recovered shear velocity at (a) Crustal depth of 10-km compared to Litho1.0 (b) Crustal depth of 20-km and compared to Litho1.0 (c) Crustal depth of 30-km (d) Moho and Sub-crustal depth of 40 km. All horizontal slices through the starting model of Litho1.0 are taken at the same depth as the new updated model. For a spatial accounting of locations where ADAMA and Litho1.0 differ see Figure S6 in Supporting Information S1.

but they do not allow a complete view of the continent. Unlike all the other models, the probabilistic approach makes it possible to use the large-ensemble statistics to evaluate resolution of various features on the continent.

We point out that not all the features in our crustal model are well resolved. This is because of the uncertainties inherited from the dispersion measurements. While this might at first be discouraging, we note that we are able to identify and quantify the total area of the entire continent that is not well resolved (Figure 7). All in all, this provides users with a quantitative judgment of how much confidence to place in the various parts of our new model update. The analyst can determine which regions are highest priorities for continued updates as new seismic measurements are assimilated. As an example, it is clear that major updates are still required for the western African craton since only a few dispersion measurements have been made in that region. Also, compared to the phase dispersion, group dispersion measurements are still only useful for regional updates of the African continental crust (cf. Figures 7b and 7c). We expect that future targets will include constraining radial anisotropy (Lin et al., 2010; Moschetti

et al., 2010a, 2010b; Ojo et al., 2017) expecially along regions where both Rayleigh and Love dispersion measurements are well resolved, for example, within the eastern and Southernmost portion of Africa.

5.2. ACE-ADAMA Compared to Other Geophysical Constraints on Africa's Crustal Structure

Compared to other regions of the world, Africa is sparsely instrumented and therefore earlier seismic models based on combined active and passive source seismics have required extensive spatial averaging (Fishwick & Bastow, 2011; Globig et al., 2016; Mooney, 2010; Stolk et al., 2013). These models are heavily spatially aliased. In particular, the models of the bulk velocity in the crust or it's thickness (Moho depth) have been conducted using several techniques that can be broadly categorized into three categories: (a) passive source seismics with sensitivity to the crust, for example, receiver functions, ambient noise, or SS reflectivity (Globig et al., 2016; Pasyanos & Nyblade, 2007; Rychert & Shearer, 2010; Tugume et al., 2013) (b) regionalized earthquake body wave tomography models with only marginal sensitivity to the crust (Boyce et al., 2021; Celli, Lebedev, Schaeffer, & Gaina, 2020), and (c) joint gravity and seismic models (Finger et al., 2021, 2022; Haas et al., 2021). Our new model is not spatially aliased. In regions with high-precision (60% of Africa: Figure 7a), we provide improved resolution on the bulk shear velocity in the crust. Improved spatial resolution relies on small aperture regional networks (Nyblade, 2015; Fadel et al., 2018; Olugboji & Xue, 2022; Yu et al., 2020). Also, the adaptive probabilistic tomography approach can adequately parameritze the velocity field without imposing strict limiting assumptions on spatial averaging or smoothness (Belhadj et al., 2018; Bodin, Sambridge, Rawlinson, & Arroucau, 2012; Sambridge et al., 2013).

5.3. Crustal Taxonomy and Surface Geology

To help with describing the most important features in the ADAMA model update, we produce a taxonomy of the entire African crust. This taxonomy is a grouping of our final velocity model into four distinct crustal types based on self-similar patterns detected across the entire model. Contrasted with classification schemes described in global crustal models (Mooney et al., 2023; Pasyanos et al., 2014) our taxonomy is not informed by surface geology, or required for data extrapolation where spatial sampling is lacking. The new crustal taxonomy we have constructed is derived exclusively from applying unsupervised machine learning algorithms on our final seismological model without imposing, a priori, any biasing geological assumption. This is justified because the dispersion maps, and the model update, reflect improved lateral sampling of the continent, with two-thirds by surface area being resolved with high precision (Figure 7). To obtain the taxonomy, we use a hybrid of the sequencer algorithm and a cluster analysis (Baron & Ménard, 2021; Lekic et al., 2012).

The sequencer algorithm is an unsupervised, graph-based, machine-learning algorithm that has been used in many applications to re-order a sequence of "data objects" (e.g., seismograms, light spectra, geophysical images). The algorithm minimizes dissimilarities between neighbors and across the entire sequence (Baron & Ménard, 2021; D. Kim et al., 2020). An appropriate measure of dissimilarity (earth-mover distance) and scale (four) allows for optimal ordering. In our application, the data objects are the 1-D shear velocity profiles at each location on the African continent (columns in Figure 12). The unordered sequence of data objects is randomly distributed along the columns of a 2-D matrix with no discernible patterns and no similarities between adjoining columns. After applying the sequencer algorithm, the entire shear velocity model is now ordered with each column being similar to its adjoining neighbors (top of Figure 12). This ordered sequence is then grouped into distinct crustal types based on the K-means clustering algorithm. K-means clustering separates the ordered velocities into distinct crustal types (C1–C4) based on how similar each velocity profile is to a representative profile. A low variance relative to the centroid (see Figure 13) ensures that each crustal type is dissimilar to the others (Ogden et al., 2019). Based on the shape of the representative velocity profiles (the centroids) a natural nomenclature for the crustal type is chosen.

The C1-type is the primitive crust because it shows very little velocity gradients, and low variance, across the entire column and is little altered to lower velocities in the shallowest crust. The C2, C3, and C4 type are the modified crust with the numbers indicating the degree of modification: least (C2), moderately (C3), and extensively (C4) modified. The modified crustal types are most dissimilar in the shallowest crust (<10 km) and sometimes in the lowermost crust (>25 km). The profiles that belong to these crustal type have slow velocities, larger variances, and larger gradients as the velocities transition to the basement rocks. The spatial patterns of the new taxonomy also reveal striking correlations to the bedrock geology even though it is not derived from it. For example, the primi-

Geochemistry, Geophysics, Geosystems

10.1029/2023GC011086

Table 4
Africa's Crustal Taxonomy Using Machine-Learning

Tectonics & geology		Area-norm Extent (%)				3 km Class avg. (km/s)					10 km Class avg. (km/s)					30 km Class avg. (km/s)					40 km Class avg. (km/s)				
(%)	Based on crustal taxonomy	C1	C2	C3	C4	C1	C2	C3	C4	A*	C1	C2	C3	C4	A*	C1	C2	C3	C4	A*	C1	C2	C3	C4	A*
18.8	I. Archean Blocks ★	37.8	16.4	7.0	1.2	3.8	3.8	3.3	2.1	3.8	3.8	3.8	3.3	2.5	3.8	4.0	4	3.6	2.7	4	4.2	4.2	3.7	3	4.2
4.5	1. West-Africa (MLS, RgS)	75	16	8	1	3.9	3.9	3.7	2.9	3.9	3.9	3.9	3.7	3.6	3.9	4.1	4	4	4.1	4.1	4.2	4.3	4.2	4.7	4.2
2.3	2. Tanzania (TC)	89	11	NA	NA	3.6	3.6	NA	NA	3.6	3.6	3.6	NA	NA	3.6	4	4	NA	NA	4	4.2	4.3	NA	NA	4.2
3.9	3. Congo (AS, BKS, GKS, KS)	70	20	9	2	3.9	3.8	3.9	3.8	3.9	3.9	3.7	3.9	3.7	3.9	4	3.9	4.3	4.2	4.1	4.2	4.1	4.6	4.8	4.3
1.4	4. Sahara Meta Craton (A4)	30	40	30	NA	3.7	3.8	3.9	NA	3.8	3.8	3.8	3.9	NA	3.8	4	4	4	NA	4	4.4	4.3	4.2	NA	4.3
2.7	5. WAfrica Mobile Zone (A5)	75	22	3	NA	3.8	4	3.7	NA	3.8	3.8	4	3.7	NA	3.8	3.9	4	4	NA	3.9	4.2	4.2	4.2	NA	4.2
4	6. KaapVaal (ZC, KpC)	41	43	15	1	3.7	3.7	3.8	3	3.7	3.7	3.7	3.7	4.2	3.7	3.9	4	4.1	4.1	4	3.9	4	4.1	4.1	4
11.4	II. Basins ●	3.1	8.9	16.7	26.2	3.8	3.8	3.7	2.7	3.4	3.8	4	3.9	3.8	3.9	3.9	4	3.9	4	4	4.1	4.1	4.1	4.3	4.2
4.2	7. Congo (bsCg)	2	13	40	45	3.6	3.9	3.6	2.8	3.3	3.6	3.9	3.8	3.8	3.8	3.8	3.9	3.9	3.9	3.9	4	4.1	4	4.1	4.1
2	8. Tindouf (bsTi)	9	9	37	45	3.8	3.7	3.7	2.8	3.3	3.8	3.6	3.9	3.8	3.8	3.9	3.9	4	4.2	4.1	4.1	4.1	4.4	4.5	4.4
5.2	9. Taoudeni (bsCg)	14	34	36	16	3.9	3.8	3.7	2.5	3.6	3.9	4.2	3.9	3.7	4	4	4.1	3.9	4.1	4	4.1	4.2	4.1	4.4	4.2
28	III. Mobile Belts ■	30.3	28	27.1	23.0	3.8	3.9	3.7	2.8	3.7	3.8	3.9	3.7	3.7	3.8	3.9	3.9	4	4	3.9	4.2	4.2	4.3	4.3	4.2
12	10. West-Africa (WAMZ)	24	36	26	14	3.8	4	3.6	2.6	3.7	3.8	4	3.8	3.6	3.8	3.9	3.9	3.9	3.9	3.9	4.2	4.2	4.3	4.2	4.2
9	11. Oub./Damara (OB, DB)	52	22	21	5	3.7	3.7	3.7	3.1	3.7	3.7	3.7	3.7	3.7	3.7	3.9	3.9	4	3.9	3.9	4.1	4.2	4.2	4.2	4.1
7	12. Other Mobile Belts (M3)	32	25	28	15	3.8	3.8	3.7	2.8	3.6	3.8	3.8	3.7	3.7	3.8	4	4	4	4.2	4	4.2	4.2	4.3	4.4	4.3
14.8	IV. Orogens ▲	14.6	12.4	13.2	23.2	3.7	3.7	3.6	2.8	3.5	3.7	3.7	3.7	3.7	3.7	4	4	4.1	4.3	4.1	4.2	4.3	4.5	4.5	4.4
1.3	13. Atlas Mountains (AtM)	19	19	33	29	3.6	3.6	3.6	3.3	3.5	3.6	3.5	3.6	3.5	3.6	3.9	3.8	3.9	4.2	4	4.6	4.6	4.6	4.6	4.6
13.5	14. East Africa (EAOZ)	33	24	22	21	3.7	3.7	3.6	2.7	3.5	3.7	3.7	3.7	3.7	3.7	4	4	4.1	4.3	4.1	4.2	4.3	4.5	4.5	4.4
27	V. Unclassified ●	14.2	33.7	36.0	26.5	3.9	3.9	3.7	2.9	3.7	3.9	3.9	3.7	3.7	3.8	4	4	3.9	4.2	4	4.2	4.2	4.3	4.5	4.3
2	15. Madagascar (Madg)	31	20	22	27	3.7	3.7	3.7	2.5	3.4	3.7	3.7	3.7	3.7	3.7	4.2	4.3	4.3	4.7	4.4	4.5	4.7	4.7	4.7	4.6
24	16. Cratons (UC, ZC)	16	37	36	11	3.9	3.9	3.7	2.9	3.7	3.9	3.9	3.7	3.7	3.8	4	4	3.9	4.2	4	4.2	4.2	4.3	4.5	4.3
1	17. Others (U3)	14	19	18	49	3.7	3.8	3.6	2.6	3.2	3.6	3.8	3.8	3.7	3.7	4	4.1	4.2	4.4	4.3	4.5	4.3	4.4	4.6	4.5
100	Total Area (Class Average)	31.8	27.8	26.0	14.4	3.8	3.8	3.6	2.7	3.6	3.8	3.9	3.7	3.5	3.8	4	4	3.9	3.8	4	4.2	4.2	4.2	4.1	4.3

Note. The nomenclature on crustal types: primitive (C1) and modified (C2–C4) crust. The modified crust is further divided into three: least (C2), moderately modified (C3) and extensively modified (C4). The acronyms for basement geology are the same as in Figure 1. The following codes are used to express larger non-contiguous domains: *A4*: The archean blocks located south east of SMC; *A5*: BNS, TS; *M3*: MB, NNB, KrB, SB, bsCd; *U3*: AF, bsCd, LB, MER, MR, OR. See a visual summary of the A*(weighted average) columns in Figure S10 in Supporting Information S1. The shadings are group summaries (same as legends in Figure 1). Each shaded row is the summary of the entries below it. A sum of all the shaded rows gives the overall summary on the last row (which is also shaded).

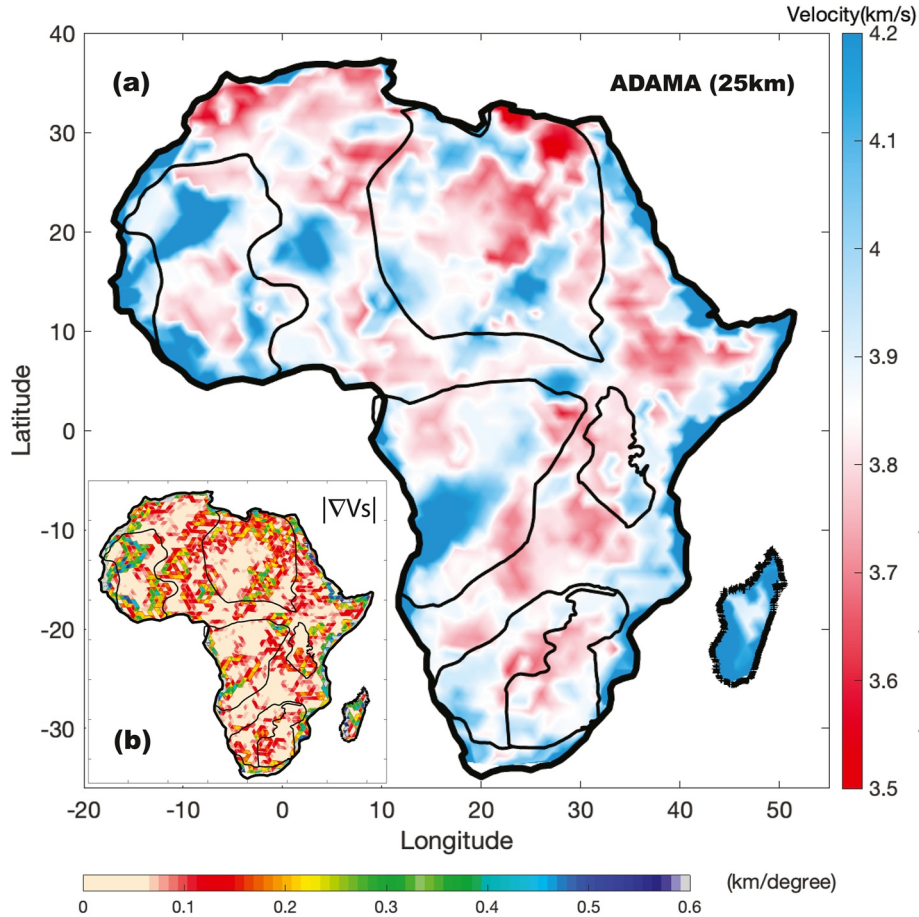

Figure 11. A view of the shear-wave velocity and 2-D horizontal gradients through the lowermost crust of Africa and Madagascar as seen by the ACE-ADAMA-RP model update. (a) The continent-wide shear wave velocities at 25 km in Africa and Madagascar. (b) The 2D-gradient of the velocity field shown in (a), highlighting the regions with the greatest changes in shear velocities: continental margins, craton edges, and the mobile belts between WAC and SMC.

tive crustal type (C1 in Figure 13) is more likely to overlap with the oldest crustal blocks in the cratons (Archean shields). By contrast, the most extensively modified crustal type (C4) is fairly consistent with basins, orogens, western margin of Madagascar, and continental margins in the North, south, and eastern margins of Africa.

5.4. Crustal Architecture: Secular Evolution, Extrapolation and Newly Resolved Features

Two broad inferences can be made based on our shear-wave velocity model and the new crustal taxonomy derived from it. The first is that a simple secular evolution of crustal genesis can-not be conclusively supported. The second is that naive extrapolations based on surface geology are not often appropriate. The inference on secular evolution is based on the correlations, and lack thereof, between the surface geology and our data-derived crustal types. Although many Archean blocks show a high spatial correlation with the primitive crustal type (C1), in other regions this is not the case. For example, the Archean terranes in the Kaapvaal cratons are a mix of multiple crustal types (C1–C3). Also, many geologically diverse regions, for example, Neoproterozoic and Archean terranes like the Oubangides belt, Kibaran belt, and the Tanzanian craton, share a similar expression of the primitive crustal types (see Tables 3 and Figure 13). While this does not rule out multiple crustal genesis models between Archean and Proterozoic terranes (Durrheim & Mooney, 1994; Thompson et al., 2010), it does favor the hypothesis that, in Africa, the crust was generated by one primary process (C1) which was then later modified (C2–C4) (Kachingwe et al., 2015; Rudnick & Gao, 2014). The processes that lead to crustal modification are most likely modulated by surface deformation—stretching, folding, thrusting or erosion—rather than

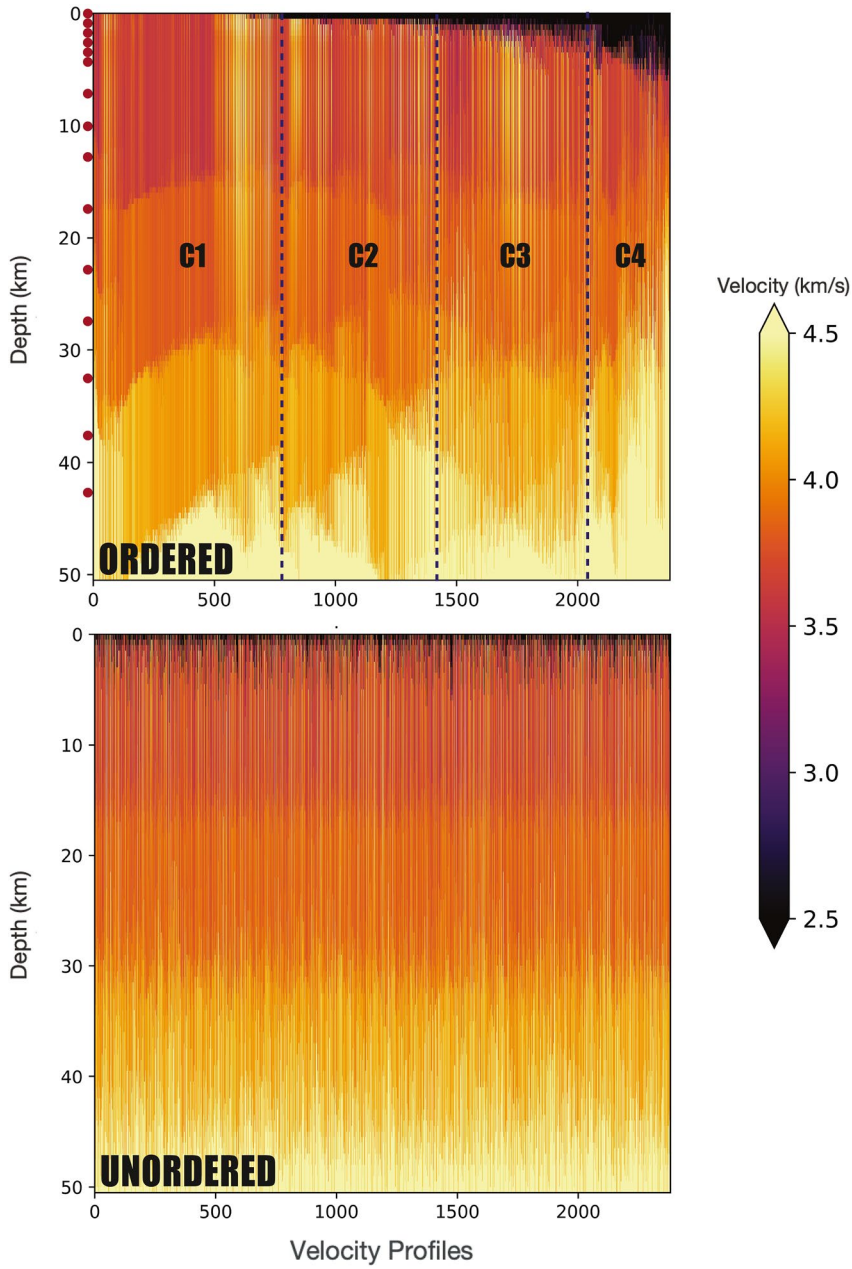

Figure 12. A crustal taxonomy obtained by sorting and grouping the ACE-ADAMA shear velocity model using an unsupervised machine learning algorithm (sequencer and K-means). (Top) The four distinct crustal types (C1–C4) obtained after sorting the velocity model along the column axis. Each crustal type is distinguished from the other by a centroid and a boundary (dashed line). The centroids (visualized in Figure 13) and the boundaries (dashed line) are obtained from running a K-means clustering algorithm on the downsampled version of the shear velocity model. The sampling interval (red dots) is along the depth-axis and is chosen to emphasize the crustal layer with the most variability, that is the shallowest crustal layer. (Bottom) The unordered shear velocity model shows random velocity distribution making it difficult to identify similarities amongst different locations. Each column is a 1-D shear velocity from a unique location in Africa and Madagascar. The ordering algorithm places similar velocity models close together based on a similarity measure after rescaling the data. The naming scheme and spatial grouping of each crystal type is provided in Figure 13 A justification for a 4-grouping scheme is provided in Figure S7 in Supporting Information S1.

mantle-mediated igneous differentiation (Hacker et al., 2015). This inference is based on the fact that the imprint of modification is mostly in the shallow and mid-crustal layers, and seems to reflect, to a large degree, late-stage deformation processes (basin formation, mountain-building, etc.). While secondary models of crustal genesis may still be possible (change in mantle temperature, or source composition), they are not extensive or distinctive

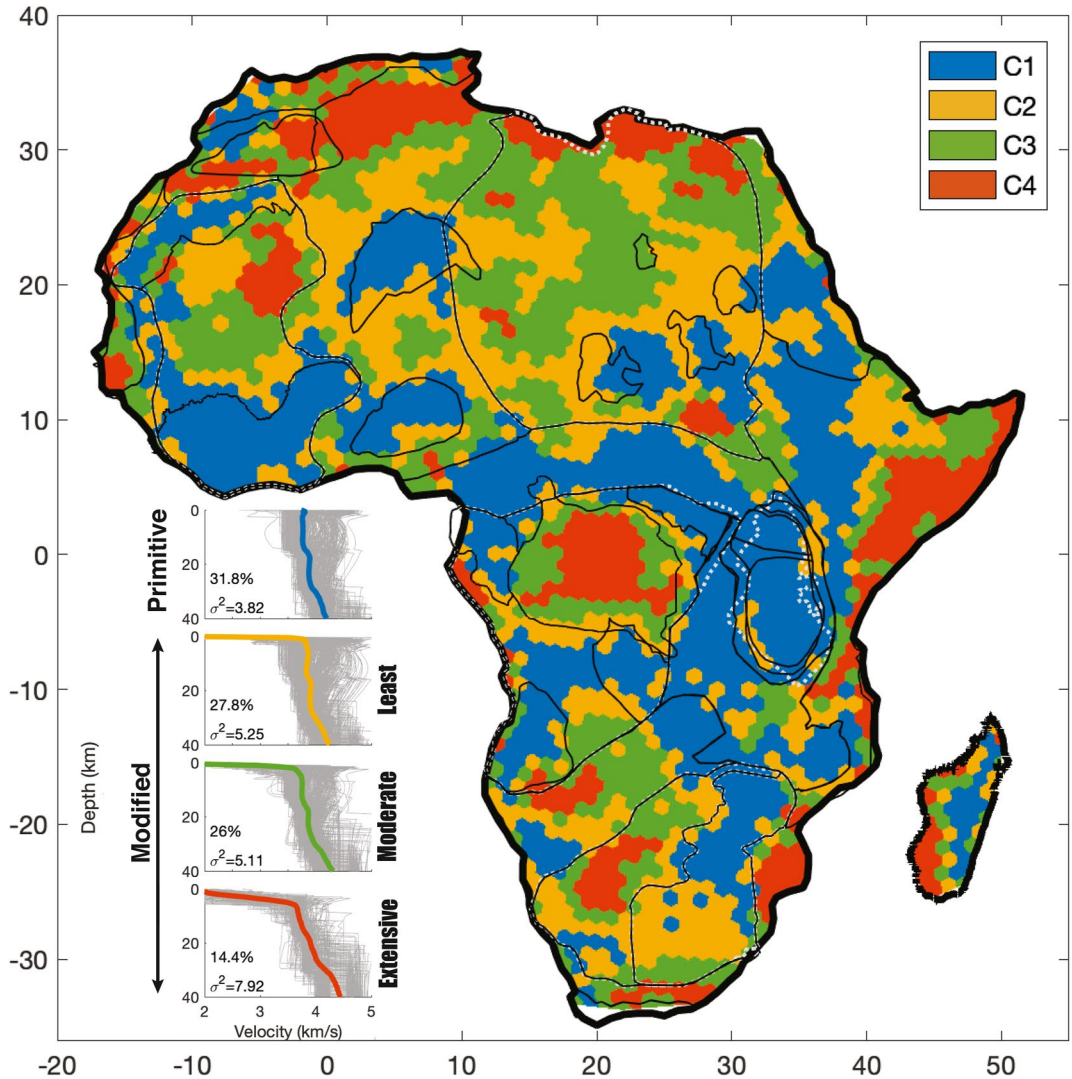

Figure 13. The crustal taxonomy overlain on the bedrock geology of Begg et al. (2009) (see also Figure 1). (Map) The locations of each of the four distinct crustal types: C1–C4. The nomenclature: primitive (C1) and modified (C2–C4) crust. The modified crust is further divided into three: least (C2), moderate (C3) and extensively modified (C4). The shear-velocity for the centroid (colored lines), distribution of all velocity profiles (gray lines), and statistics (variance relative to the centroid) of each of the crustal types are shown to the left of the map. A description of sub-groups is also provided in Figure S8 in Supporting Information S1 and a comparison between the taxonomy provided here, and other crustal classification schemes is provided in Figure S9 in Supporting Information S1.

enough to leave their imprint in the shear-velocity signal and hence are not currently detected by our crustal taxonomy. We emphasize however that this conclusion needs to be further tested when improved continent-wide models on crustal thickness and Poisson ratio are obtained following joint analysis of body-wave and surface-wave data (Abbott et al., 2013).

Our analysis suggests that much of Africa's crust is a statistical mix of two main crustal types: primitive (one third by area) and modified (two-thirds by area) crust. All the crustal types share some commonalities: they have similar mid and lower crustal velocities which are statistically comparable within variance. However, they also retain some clear differences. The primitive crust has faster velocities within the entire crustal column and tighter variances with little differences in the top and bottom layers of the crust (moderate gradients). Because of this pattern, much of the Archean blocks are faster on average, especially in the shallowest crust. The clearest expression of this behavior is the Archean shields in West Africa which possess the fastest shear-wave velocities on the continent (see Table 4 and Figure S10 in Supporting Information S1). As the crust evolves and is modified, much

of the variation in shear-wave velocities is taken up in the shallowest layers and leads to more variation across the entire crustal column. For example, the least and moderately modified crustal types (C2 and C3) are evenly expressed across Africa and preserve larger gradients in the topmost crust and moderate gradients in the lower crust (Figure 13 and Figure S7 in Supporting Information S1).

Taken together, our new shear velocity model, when synthesized with the crustal taxonomy, show newly resolved features across the continent, including but not limited to: (a) C1-type dominated crust in the Archean shields of the West-Africa, Congo and south-east of the Sahara Meta Craton (b) C3 and C4-dominated crust in the basins and along the eastern margins of Africa (c) A more heterogeneous Kaapvaal craton in Southern Africa compared to the other cratons (see also Table 4) and (d) a crustal taxonomy that is largely different from existing schemes (Figure S8 in Supporting Information S1). Some of these features, though visible in the velocity model (Figures 10 and 11), are more clearly captured by the machine learning algorithm (Figure 13 and Table 4). The fact that we can make continent-wide inferences is justified by highly precise Rayleigh wave dispersion measurements (Figures 2b, 5c2, and 4d2) and therefore the newly resolved features can be interpreted with better confidence. Compared with the reference model, Litho1.0, the shear-wave velocities are faster within the exposed Archean shields, along the continental margins, and especially for a few of the craton edges (compare Figure 10b2 with Figure 11). In particular, as already argued, the outlines of the Archean shields in the west African craton and the Congo craton are much more prominent and are now clearly delineated with our crustal taxonomy (Begg et al., 2009). The spatial homogeneity of some of these features are clearly seen in the taxonomy even with coherent features detectable along highly mobile belts between the west African craton and the Sahara Meta Craton. We expect that future work will apply our model and taxonomy to other geological and geophysical problems, for example, improving constraining crustal composition (Afonso et al., 2022; Hacker et al., 2015; Sammon et al., 2022; Sammon & McDonough, 2021), lithospheric stress modeling (Craig et al., 2011; Stamps et al., 2010; Zoback & Mooney, 2003), and connection to long-term deformation and seismicity on the African continent (Fadel et al., 2020; Schmandt et al., 2015).

6. Conclusion

We construct a new shear-wave velocity model of Africa's crustal architecture using a probabilistic and perturbational inversion of ambient noise surface wave measurements. The probabilistic inversion solves for phase and group dispersion maps using a transdimensional and hierarchical Bayesian inversion of a large catalog of interstation dispersion data. The dispersion map are large ensemble models of a posterior distribution and provide estimates of statistical significance. An evaluation of the error statistics suggests that the phase dispersion is better constrained than group dispersion, with Rayleigh wave phase dispersion maps possessing the best resolution. Informed by these error statistics, we use a perturbational approach to construct the updated model of Africa's crustal architecture evaluated using the Rayleigh phase maps and starting from a reference global model (Litho 1.0). The model recovers new features not present in existing maps, with important implications for crustal structure and geological architecture of Archean cratons, exposed shields and mobile belts within Africa.

Data Availability Statement

No seismic data was used in this study. The full catalog of dispersion measurements can be obtained from Xue and Olugboji (2021) and was published alongside (Olugboji & Xue, 2022). A digital format of the probabilistic surface wave dispersion maps and the shear velocity model of Africa's Crust Evaluated using the ADAMA Rayleigh wave Phase dispersion (ACE-ADAMA-RP) is available at (Xue, 2023).

Acknowledgments
This work was made possible by the National Science Foundation under Grant 2102495. We thank the Incorporated Research Institutions for Seismology, whose internship program allowed Tamama to pursue this research We thank Siyu Xue, for computing the ambient noise cross correlations for all station pairs and providing us with the Love and Rayleigh wave dispersion measurements crucial to this project. We thank Baowei Liu for his assistance in preparing our inversions. We thank the University of Rochester's Center for Integrated Research Computing (CIRC), for providing us with the computational support and resources for this project. We also thank Carl Schmidtman and Miki Nakajima for generously allocating us with additional computational resources. We acknowledge many helpful discussions with Lara Wagner, Baowei Liu, Ziqi Zhang, Walter Hennings, Enting Zhou, Sayan Swar, Steve Carr, Canberk Eckmecki. This work used Bridges2 at Pittsburgh Supercomputing Center (PSC) and Expanse at San Diego Supercomputer Center (SDSC) through allocation EES220030 from the Advanced Cyberinfrastructure Coordination Ecosystem: Services & Support (ACCESS) program Boerner et al. (2023), which is supported by National Science Foundation Grants #2138259, #2138286, #2138307, #2137603, and #2138296.

References

Abbott, D. H., Mooney, W. D., & VanTongeren, J. A. (2013). The character of the Moho and lower crust within Archean cratons and the tectonic implications. *Tectonophysics*, *609*, 690–705. https://doi.org/10.1016/j.tecto.2013.09.014

Accardo, N. J., Gaherty, J. B., Shillington, D. J., Ebinger, C. J., Nyblade, A. A., Mbogoni, G. J., et al. (2017). Surface wave imaging of the weakly extended Malawi rift from ambient-noise and teleseismic Rayleigh waves from onshore and lake-bottom seismometers. *Geophysical Journal International*, *209*(3), 1892–1905. https://doi.org/10.1093/gji/ggx133

Adams, A., & Nyblade, A. (2011). Shear wave velocity structure of the southern African upper mantle with implications for the uplift of southern Africa. *Geophysical Journal International*, *186*(2), 808–824. https://doi.org/10.1111/j.1365-246x.2011.05072.x

Afonso, J. C., Ben-Mansour, W., O'Reilly, S. Y., Griffin, W. L., Salajeghegh, F., Foley, S., et al. (2022). Thermochemical structure and evolution of cratonic lithosphere in central and southern Africa. *Nature Geoscience*, *15*(5), 405–410. https://doi.org/10.1038/s41561-022-00929-y

Baron, D., & Ménard, B. (2021). Extracting the main trend in a data set: The sequencer algorithm. *The Astrophysical Journal*, *916*(2), 91. https://doi.org/10.3847/1538-4357/abfc4d

Begg, G. C., Griffin, W. L., Natapov, L. M., O'Reilly, S. Y., Grand, S. P., O'Neill, C. J., & Bowden, P. (2009). The lithospheric architecture of Africa: Seismic tomography, mantle petrology, and tectonic evolution. *Geosphere*, *5*(1), 23–50. https://doi.org/10.1130/ges00179.s2

Behn, M. D., Lin, J., & Zuber, M. T. (2002). A continuum mechanics model for normal faulting using a strain-rate softening rheology: Implications for thermal and rheological controls on continental and oceanic rifting. *Earth and Planetary Science Letters*, *202*(3), 725–740. https://doi.org/10.1016/s0012-821x(02)00792-6

Belhadj, J., Romary, T., Gesret, A., Noble, M., & Figliuzzi, B. (2018). New parameterizations for Bayesian seismic tomography. *Inverse Problems*, *34*(6), 065007. https://doi.org/10.1088/1361-6420/aabce7

Bodin, T., & Sambridge, M. (2009). Seismic tomography with the reversible jump algorithm. *Geophysical Journal International*, *178*(3), 1411–1436. https://doi.org/10.1111/j.1365-246x.2009.04226.x

Bodin, T., Sambridge, M., & Gallagher, K. (2009). A self-parametrizing partition model approach to tomographic inverse problems. *Inverse Problems*, *25*(5), 055009. https://doi.org/10.1088/0266-5611/25/5/055009

Bodin, T., Sambridge, M., Rawlinson, N., & Arroucau, P. (2012). Transdimensional tomography with unknown data noise. *Geophysical Journal International*, *189*(3), 1536–1556. https://doi.org/10.1111/j.1365-246x.2012.05414.x

Bodin, T., Sambridge, M., Tkalčić, H., Arroucau, P., Gallagher, K., & Rawlinson, N. (2012). Transdimensional inversion of receiver functions and surface wave dispersion. *Journal of Geophysical Research*, *117*(B2), B02301. https://doi.org/10.1029/2011jb008560

Boerner, T. J., Deems, S., Furlani, T. R., Knuth, S. L., & Towns, J. (2023). ACCESS: Advancing Innovation: NSF's Advanced Cyberinfrastructure Coordination Ecosystem: Services & Support. In *Practice and Experience in Advanced Research Computing (PEARC '23)", Portland, OR, USA*. ACM, 4. https://doi.org/10.1145/3569951.3597559

Borrego, D., Nyblade, A. A., Accardo, N. J., Gaherty, J. B., Ebinger, C. J., Shillington, D. J., et al. (2018). Crustal structure surrounding the northern Malawi rift and beneath the Rungwe volcanic province, east Africa. *Geophysical Journal*, *215*(2), 1410–1426. https://doi.org/10.1093/gji/ggy331

Boyce, A., Bastow, I. D., Cottaar, S., Kounoudis, R., Guilloud De Courbeville, J., Caunt, E., & Desai, S. (2021). AFRP20: New P-wavespeed model for the African mantle reveals two whole-mantle plumes below east Africa and Neoproterozoic modification of the Tanzania craton. *Geochemistry, Geophysics, Geosystems*, *22*(3), e2020GC009302. https://doi.org/10.1029/2020gc009302

Brocher, T. M. (2005). Empirical relations between elastic wavespeeds and density in the Earth's crust. *Bulletin of the Seismological Society of America*, *95*(6), 2081–2092. https://doi.org/10.1785/0120050077

Buehler, J. S., & Shearer, P. M. (2017). Uppermost mantle seismic velocity structure beneath USArray. *Journal of Geophysical Research: Solid Earth*, *122*(1), 436–448. https://doi.org/10.1002/2016jb013265

Burke, K., & Gunnell, Y. (2008). The African erosion surface: A Continental-Scale synthesis of geomorphology, tectonics, and environmental. In *Memoir 201: The African erosion surface: A continental-scale synthesis of geomorphology, tectonics, and environmental change over the past 180 million years* (Vol. 201, pp. 1–66). Geological Society of America.

Celli, N. L., Lebedev, S., Schaeffer, A. J., & Gaina, C. (2020). African cratonic lithosphere carved by mantle plumes. *Nature Communications*, *11*(1), 92. https://doi.org/10.1038/s41467-019-13871-2

Celli, N. L., Lebedev, S., Schaeffer, A. J., Ravenna, M., & Gaina, C. (2020). The upper mantle beneath the South Atlantic Ocean, South America and Africa from waveform tomography with massive data sets. *Geophysical Journal International*, *221*(1), 178–204. https://doi.org/10.1093/gji/ggz574

Chambers, E. L., Harmon, N., Keir, D., & Rychert, C. A. (2019). Using ambient noise to image the northern east African rift. *Geochemistry, Geophysics, Geosystems*, *20*(4), 2091–2109. https://doi.org/10.1029/2018gc008129

Chorowicz, J. (2005). The east African rift system. *Journal of African Earth Sciences*, *43*(1), 379–410. https://doi.org/10.1016/j.jafrearsci.2005.07.019

Craig, T. J., Jackson, J. A., Priestley, K., & McKenzie, D. (2011). Earthquake distribution patterns in Africa: Their relationship to variations in lithospheric and geological structure, and their rheological implications. *Geophysical Journal International*, *185*(1), 403–434. https://doi.org/10.1111/j.1365-246x.2011.04950.x

Crosby, A. G., Fishwick, S., & White, N. (2010). Structure and evolution of the intracratonic Congo basin. *Geochemistry, Geophysics, Geosystems*, *11*(6), Q06010. https://doi.org/10.1029/2009gc003014

Crowder, E., Rawlinson, N., Pilia, S., Cornwell, D. G., & Reading, A. M. (2019). Transdimensional ambient noise tomography of Bass Strait, southeast Australia, reveals the sedimentary basin and deep crustal structure beneath a failed continental rift. *Geophysical Journal International*, *217*(2), 970–987. https://doi.org/10.1093/gji/ggz057

Doucouré, C. M., & de Wit, M. J. (2003). Old inherited origin for the present near-bimodal topography of Africa. *Journal of African Earth Sciences*, *36*(4), 371–388. https://doi.org/10.1016/s0899-5362(03)00019-8

Durrheim, R. J., & Mooney, W. D. (1994). Evolution of the Precambrian lithosphere: Seismological and geochemical constraints. *Journal of Geophysical Research*, *99*(B8), 15359–15374. https://doi.org/10.1029/94jb00138

Emry, E. L., Shen, Y., Nyblade, A. A., Flinders, A., & Bao, X. (2019). Upper mantle earth structure in Africa from Full-Wave ambient noise tomography. *Geochemistry, Geophysics, Geosystems*, *20*(1), 120–147. https://doi.org/10.1029/2018gc007804

Eshetu, A., Mammo, T., & Tilmann, F. (2021). Imaging the Ethiopian rift region using transdimensional hierarchical seismic noise tomography. *Pure and Applied Geophysics*, *178*(11), 4367–4388. https://doi.org/10.1007/s00024-021-02880-2

Fadel, I., Paulssen, H., van der Meijde, M., Kwadiba, M., Ntibinyane, O., Nyblade, A., & Durrheim, R. (2020). Crustal and upper mantle shear wave velocity structure of Botswana: The 3 April 2017 central Botswana earthquake linked to the east African rift system. *Geophysical Research Letters*, *47*(4), e2019GL085598. https://doi.org/10.1029/2019gl085598

Fadel, I., van der Meijde, M., & Paulssen, H. (2018). Crustal structure and dynamics of Botswana. *Journal of Geophysical Research: Solid Earth*, *123*(12), 10659–10671. https://doi.org/10.1029/2018jb016190

Finger, N.-P., Kaban, M. K., Tesauro, M., Mooney, W. D., & Thomas, M. (2021). *Thermo-compositional model of cratonic lithosphere and depth to Moho of Africa*. GFZ Data Services.

Finger, N.-P., Kaban, M. K., Tesauro, M., Mooney, W. D., & Thomas, M. (2022). A thermo-compositional model of the African cratonic lithosphere. *Geochemistry, Geophysics, Geosystems*, *23*(3), e2021GC010296. https://doi.org/10.1029/2021gc010296

Fishwick, S., & Bastow, I. D. (2011). Towards a better understanding of African topography: A review of passive-source seismic studies of the African crust and upper mantle. *Geological Society, London, Special Publications*, *357*(1), 343–371. https://doi.org/10.1144/sp357.19

Galetti, E., Curtis, A., Baptie, B., Jenkins, D., & Nicolson, H. (2016). Transdimensional love-wave tomography of the British Isles and shear-velocity structure of the east Irish Sea basin from ambient-noise interferometry. *Geophysical Journal International*, *208*(1), 36–58. https://doi.org/10.1093/gji/ggw286

Gao, L., Zhang, H., Gao, L., He, C., Xin, H., & Shen, W. (2022). High-resolution vs tomography of south China by joint inversion of body wave and surface wave data. *Tectonophysics*, *824*, 229228. https://doi.org/10.1016/j.tecto.2022.229228
Globig, J., Fernàndez, M., Torne, M., Vergés, J., Robert, A., & Faccenna, C. (2016). New insights into the crust and lithospheric mantle structure of Africa from elevation, geoid, and thermal analysis. *Journal of Geophysical Research: Solid Earth*, *121*(7), 5389–5424. https://doi.org/10.1002/2016jb012972
Haas, P., Ebbing, J., Celli, N. L., & Rey, P. F. (2021). Two-step gravity inversion reveals variable architecture of African cratons. *Frontiers of Earth Science in China*, *9*, 1240. https://doi.org/10.3389/feart.2021.696674
Haas, P., Ebbing, J., & Szwillus, W. (2020). Sensitivity analysis of gravity gradient inversion of the Moho depth—A case example for the Amazonian craton. *Geophysical Journal International*, *221*(3), 1896–1912. https://doi.org/10.1093/gji/ggaa122
Hacker, B. R., Kelemen, P. B., & Behn, M. D. (2012). Continental lower crust. *Annual Review of Earth and Planetary Sciences*, *43*(1), 167–205. https://doi.org/10.1146/annurev-earth-050212-124117
Hacker, B. R., Kelemen, P. B., & Behn, M. D. (2015). Continental lower crust. *Annual Review of Earth and Planetary Sciences*, *43*(1), 167–205. https://doi.org/10.1146/annurev-earth-050212-124117
Han, S., Zhang, H., Xin, H., Shen, W., & Yao, H. (2022). USTClitho2.0: Updated unified seismic tomography models for continental China lithosphere from joint inversion of body-wave arrival times and surface-wave dispersion data. *Seismological Research Letters*, *93*(1), 201–215. https://doi.org/10.1785/0220210122
Haney, M. M., & Tsai, V. C. (2017). Perturbational and nonperturbational inversion of Rayleigh-wave velocities. *Geophysics*, *82*(3), F15–F28. https://doi.org/10.1190/geo2016-0397.1
Haney, M. M., & Tsai, V. C. (2020). Perturbational and nonperturbational inversion of love-wave velocities. *Geophysics*, *85*(1), F19–F26. https://doi.org/10.1190/geo2018-0882.1
Hawkins, R., Bodin, T., Sambridge, M., Choblet, G., & Husson, L. (2019). Trans-dimensional surface reconstruction with different classes of parameterization. *Geochemistry: Exploration, Environment, Analysis*, *20*(1), 505–529. https://doi.org/10.1029/2018gc008022
Hawkins, R., & Sambridge, M. (2019). An adjoint technique for estimation of interstation phase and group dispersion from ambient noise cross correlations. *Bulletin of the Seismological Society of America*, *109*(5), 1716–1728. https://doi.org/10.1785/0120190060
Jessell, M. W., Begg, G. C., & Miller, M. S. (2016). The geophysical signatures of the west African craton. *Precambrian Research*, *274*, 3–24. https://doi.org/10.1016/j.precamres.2015.08.010
Kachingwe, M., Nyblade, A., & Julia, J. (2015). Crustal structure of Precambrian terranes in the southern African subcontinent with implications for secular variation in crustal genesis. *Geophysical Journal International*, *202*(1), 533–547. https://doi.org/10.1093/gji/ggv136
Kim, D., Lekić, V., Ménard, B., Baron, D., & Taghizadeh-Popp, M. (2020). Sequencing seismograms: A panoptic view of scattering in the core-mantle boundary region. *Science*, *368*(6496), 1223–1228. https://doi.org/10.1126/science.aba8972
Kim, S., Nyblade, A. A., Rhie, J., Baag, C.-E., & Kang, T.-S. (2012). Crustal s-wave velocity structure of the main Ethiopian rift from ambient noise tomography. *Geophysical Journal International*, *191*(2), 865–878. https://doi.org/10.1111/j.1365-246x.2012.05664.x
Laske, G., Masters, G., Ma, Z., & Pasyanos, M. (2013). Update on CRUST1.0 - A 1-degree global model of Earth's crust. *Geophysical Research Abstracts*, *15*. Abstract EGU2013-2658.
Lebedev, S., Adam, J. M.-C., & Meier, T. (2013). Mapping the Moho with seismic surface waves: A review, resolution analysis, and recommended inversion strategies. *Tectonophysics*, *609*, 377–394. https://doi.org/10.1016/j.tecto.2012.12.030
Lekic, V., Cottaar, S., Dziewonski, A., & Romanowicz, B. (2012). Cluster analysis of global lower mantle tomography: A new class of structure and implications for chemical heterogeneity. *Earth and Planetary Science Letters*, *357*, 68–77. https://doi.org/10.1016/j.epsl.2012.09.014
Li, A., & Burke, K. (2006). Upper mantle structure of southern Africa from Rayleigh wave tomography. *Journal of Geophysical Research*, *111*(B10). https://doi.org/10.1029/2006jb004321
Lin, F.-C., Ritzwoller, M. H., & Snieder, R. (2009). Eikonal tomography: Surface wave tomography by phase front tracking across a regional broad-band seismic array. *Geophysical Journal International*, *177*(3), 1091–1110. https://doi.org/10.1111/j.1365-246x.2009.04105.x
Lin, F.-C., Ritzwoller, M. H., Yang, Y., Moschetti, M. P., & Fouch, M. J. (2010). Complex and variable crustal and uppermost mantle seismic anisotropy in the western United States. *Nature Geoscience*, *4*(1), 55–61. https://doi.org/10.1038/ngeo1036
Lithgow-Bertelloni, C., & Silver, P. G. (1998). Dynamic topography, plate driving forces and the African superswell. *Nature*, *395*(6699), 269–272. https://doi.org/10.1038/26212
Lowry, A. R., & Pérez-Gussinyé, M. (2011). The role of crustal quartz in controlling cordilleran deformation. *Nature*, *471*(7338), 353–357. https://doi.org/10.1038/nature09912
Lu, Y., Stehly, L., & Paul, A. (2018). High-resolution surface wave tomography of the European crust and uppermost mantle from ambient seismic noise. *Geophysical Journal International*, *214*(2), 1136–1150. https://doi.org/10.1093/gji/ggy188
Malinverno, A., & Briggs, V. A. (2004). Expanded uncertainty quantification in inverse problems: Hierarchical Bayes and empirical Bayes. *Geophysics*, *69*(4), 1005–1016. https://doi.org/10.1190/1.1778243
Malory, A. O., Bao, X., & Chen, Z. (2022). Crustal shear wave velocity and radial anisotropy beneath southern Africa from ambient noise tomography. *Tectonophysics*, *822*, 229191. https://doi.org/10.1016/j.tecto.2021.229191
Min, G., & Hou, G. (2019). Mechanism of the mesozoic African rift system: Paleostress field modeling. *Journal of Geodynamics*, *132*, 101655. https://doi.org/10.1016/j.jog.2019.101655
Molinari, I., & Morelli, A. (2011). EPcrust: A reference crustal model for the European plate. *Geophysical Journal International*, *185*(1), 352–364. https://doi.org/10.1111/j.1365-246x.2011.04940.x
Mooney, W. D. (2010). Crust and lithospheric structure–global crustal structure. In *Treatise on geophysics* (Vol. 1, p. 361). Unknown.
Mooney, W. D., Barrera-Lopez, C., Suárez, M. G., & Castelblanco, M. A. (2023). Earth crustal model 1 (ECM1): A 1° x 1° global seismic and density model. *Earth-Science Reviews*, *243*, 104493. https://doi.org/10.1016/j.earscirev.2023.104493
Moschetti, M. P., Ritzwoller, M. H., Lin, F., & Yang, Y. (2010a). Seismic evidence for widespread western-US deep-crustal deformation caused by extension. *Nature*, *464*(7290), 885–889. https://doi.org/10.1038/nature08951
Moschetti, M. P., Ritzwoller, M. H., Lin, F.-C., & Yang, Y. (2010b). Crustal shear wave velocity structure of the western United States inferred from ambient seismic noise and earthquake data. *Journal of Geophysical Research*, *115*(July), 1–20. https://doi.org/10.1029/2010jb007448
Nair, S. K., Gao, S. S., Liu, K. H., & Silver, P. G. (2006). Southern African crustal evolution and composition: Constraints from receiver function studies. *Journal of Geophysical Research*, *111*(B2), B02304. https://doi.org/10.1029/2005jb003802
Nyblade, A. (2015). Nyblade, a (2015) Africaarray-Namibia [Dataset]. https://doi.org/10.7914/SN/8A_2015
Ogden, C., Bastow, I. D., Gilligan, A., & Rondenay, S. (2019). A reappraisal of the h–κ stacking technique: Implications for global crustal structure. *Geophysical Journal International*, *219*(3), 1491–1513. https://doi.org/10.1093/gji/ggz364
Ojo, A. O., Ni, S., & Li, Z. (2017). Crustal radial anisotropy beneath Cameroon from ambient noise tomography. *Tectonophysics*, *696–697*, 37–51. https://doi.org/10.1016/j.tecto.2016.12.018

Olugboji, T., & Xue, S. (2022). A short-period surface-wave dispersion dataset for model assessment of Africa's crust: ADAMA. *Bulletin of the Seismological Society of America*, *93*(3), 1943–1959. https://doi.org/10.1785/0220210355

Olugboji, T., Lekic, V., & McDonough, W. (2017). A statistical assessment of seismic models of the U.S. continental crust using Bayesian inversion of ambient noise surface wave dispersion data. *Tectonics*, *36*(7), 1232–1253. https://doi.org/10.1002/2017tc004468

Pasyanos, M. E., Masters, T. G., Laske, G., & Ma, Z. (2014). LITHO1.0: An updated crust and lithospheric model of the earth. *Journal of Geophysical Research: Solid Earth*, *119*(3), 2153–2173. https://doi.org/10.1002/2013jb010626

Pasyanos, M. E., & Nyblade, A. A. (2007). A top to bottom lithospheric study of Africa and Arabia. *Tectonophysics*, *444*(1), 27–44. https://doi.org/10.1016/j.tecto.2007.07.008

Pilia, S., Jackson, J. A., Hawkins, R., Kaviani, A., & Ali, M. Y. (2020). The southern Zagros collisional Orogen: New insights from transdimensional trees inversion of seismic noise. *Geophysical Research Letters*, *47*(4), e2019GL086258. https://doi.org/10.1029/2019gl086258

Raveloson, A., Nyblade, A., & Durrheim, R. (2021). Joint inversion of surface wave and gravity data reveals subbasin architecture of the Congo basin. *Geology*, *49*(7), 810–815. https://doi.org/10.1130/g48408.1

Raveloson, A., Nyblade, A., Fishwick, S., Mangongolo, A., & Master, S. (2015). The upper mantle seismic velocity structure of South-Central Africa and the seismic architecture of Precambrian lithosphere beneath the Congo basin. In M. J. deWit, F. Guillocheau, & M. C. J. deWit (Eds.), *Geology and resource potential of the Congo basin* (pp. 3–18). Springer Berlin Heidelberg.

Rawlinson, N., Pilia, S., Young, M., Salmon, M., & Yang, Y. (2016). Crust and upper mantle structure beneath southeast Australia from ambient noise and teleseismic tomography. *Tectonophysics*, *689*, 143–156. https://doi.org/10.1016/j.tecto.2015.11.034

Roux, P., Sabra, K. G., Kuperman, W. A., & Roux, A. (2005). Ambient noise cross correlation in free space: Theoretical approach. *Journal of the Acoustical Society of America*, *117*(1), 79–84. https://doi.org/10.1121/1.1830673

Rudnick, R. L., & Gao, S. (2014). Composition of the continental crust. In *Treatise on geochemistry* (2nd ed., Vol. 4, pp. 1–51). Elsevier.

Rychert, C. A., & Shearer, P. M. (2010). Resolving crustal thickness using SS waveform stacks. *Geophysical Journal International*, *180*(3), 1128–1137. https://doi.org/10.1111/j.1365-246x.2009.04497.x

Sambridge, M., Bodin, T., Gallagher, K., & Tkalcic, H. (2013). Transdimensional inference in the geosciences. *Philosophical Transactions of the Royal Society A*, *371*(1984), 20110547. https://doi.org/10.1098/rsta.2011.0547

Sambridge, M., Braun, J., & McQueen, H. (1995). Geophysical parametrization and interpolation of irregular data using natural neighbours. *Geophysical Journal International*, *122*(3), 837–857. https://doi.org/10.1111/j.1365-246x.1995.tb06841.x

Sammon, L. G., & McDonough, W. F. (2021). A geochemical review of amphibolite, granulite, and eclogite facies lithologies: Perspectives on the deep continental crust. *Journal of Geophysical Research: Solid Earth*, *126*(12). e2021JB022791. https://doi.org/10.1029/2021jb022791

Sammon, L. G., Mcdonough, W. F., & Mooney, W. D. (2022). Compositional attributes of the deep continental crust inferred from geochemical and geophysical data. *Journal of Geophysical Research: Solid Earth*, *127*(8), e2022JB024041.

Saygin, E., & Kennett, B. L. N. (2012). Crustal structure of Australia from ambient seismic noise tomography. *Journal of Geophysical Research*, *117*(B1), B01304. https://doi.org/10.1029/2011jb008403

Schmandt, B., Lin, F.-C., & Karlstrom, K. E. (2015). Distinct crustal isostasy trends east and west of the rocky mountain front. *Geophysical Research Letters*, *42*(23), 10290–10298. https://doi.org/10.1002/2015gl066593

Schutt, D. L., Lowry, A. R., & Buehler, J. S. (2018). Moho temperature and mobility of lower crust in the western United States. *Geology*, *46*(3), 219–222. https://doi.org/10.1130/g39507.1

Shen, W., & Ritzwoller, M. H. (2016). Crustal and uppermost mantle structure beneath the United States. *Journal of Geophysical Research: Solid Earth*, *121*(6), 4306–4342. https://doi.org/10.1002/2016jb012887

Shen, W., Ritzwoller, M. H., Kang, D., Kim, Y., Lin, F.-C., Ning, J., et al. (2016). A seismic reference model for the crust and uppermost mantle beneath China from surface wave dispersion. *Geophysical Journal International*, *206*(2), 954–979. https://doi.org/10.1093/gji/ggw175

Shen, W., Ritzwoller, M. H., Schulte-Pelkum, V., & Lin, F.-C. (2012). Joint inversion of surface wave dispersion and receiver functions: A Bayesian Monte-Carlo approach. *Geophysical Journal International*, *192*(2), 807–836. https://doi.org/10.1093/gji/ggs050

Shen, W., Wiens, D. A., Anandakrishnan, S., Aster, R. C., Gerstoft, P., Bromirski, P. D., et al. (2018). The crust and upper mantle structure of central and west Antarctica from Bayesian inversion of Rayleigh wave and receiver functions. *Journal of Geophysical Research: Solid Earth*, *123*(9), 7824–7849. https://doi.org/10.1029/2017jb015346

Shinevar, W. J., Behn, M. D., & Hirth, G. (2015). Compositional dependence of lower crustal viscosity. *Geophysical Research Letters*, *42*(20), 8333–8340. https://doi.org/10.1002/2015gl065459

Shinevar, W. J., Behn, M. D., Hirth, G., & Jagoutz, O. (2018). Inferring crustal viscosity from seismic velocity: Application to the lower crust of southern California. *Earth and Planetary Science Letters*, *494*, 83–91. https://doi.org/10.1016/j.epsl.2018.04.055

Stamps, D. S., Flesch, L. M., & Calais, E. (2010). Lithospheric buoyancy forces in Africa from a thin sheet approach. *International Journal of Earth Sciences*, *99*(7), 1525–1533. https://doi.org/10.1007/s00531-010-0533-2

Stolk, W., Kaban, M., Beekman, F., Tesauro, M., Mooney, W. D., & Cloetingh, S. (2013). High resolution regional crustal models from irregularly distributed data: Application to Asia and adjacent areas. *Tectonophysics*, *602*, 55–68. https://doi.org/10.1016/j.tecto.2013.01.022

Thompson, D., Bastow, I., Helffrich, G., Kendall, J., Wookey, J., Snyder, D., & Eaton, D. (2010). Precambrian crustal evolution: Seismic constraints from the Canadian Shield. *Earth and Planetary Science Letters*, *297*(3–4), 655–666. https://doi.org/10.1016/j.epsl.2010.07.021

Trabant, C., Hutko, A. R., Bahavar, M., Karstens, R., Ahern, T., & Aster, R. (2012). Data products at the IRIS DMC: Stepping stones for research and other applications. *Seismological Research Letters*, *83*(5), 846–854. https://doi.org/10.1785/0220120032

Tugume, F., Nyblade, A., Julià, J., & van der Meijde, M. (2013). Precambrian crustal structure in Africa and Arabia: Evidence lacking for secular variation. *Tectonophysics*, *609*, 250–266. https://doi.org/10.1016/j.tecto.2013.04.027

Wang, T., Feng, J., Liu, K. H., & Gao, S. S. (2019). Crustal structure beneath the Malawi and Luangwa rift zones and adjacent areas from ambient noise tomography. *Gondwana Research*, *67*, 187–198. https://doi.org/10.1016/j.gr.2018.10.018

White-Gaynor, A. L., Nyblade, A. A., Durrheim, R. J., Raveloson, R., van der Meijde, M., Fadel, I., et al. (2021). Shear-wave velocity structure of the southern African upper mantle: Implications for craton structure and plateau uplift. *Geophysical Research Letters*, *48*(7), e2020GL091624. https://doi.org/10.1029/2020gl091624

Wipperfurth, S. A., Šrámek, O., & McDonough, W. F. (2020). Reference models for lithospheric geoneutrino signal. *Journal of Geophysical Research: Solid Earth*, *125*(2), e2019JB018433. https://doi.org/10.1029/2019jb018433

Xue, S. (2023). Urseismology/ace_adama: Ace_adama. *Zenodo*. https://doi.org/10.5281/zenodo.8017902

Xue, S., & Olugboji, T. (2021). URseismology/ADAMA: ADAMA.1.

Yang, Y., Li, A., & Ritzwoller, M. H. (2008). Crustal and uppermost mantle structure in southern Africa revealed from ambient noise and teleseismic tomography. *Geophysical Journal International*, *174*(1), 235–248. https://doi.org/10.1111/j.1365-246x.2008.03779.x

Yu, Y., Gao, S. S., Zhao, D., & Liu, K. H. (2020). Mantle structure and flow beneath an early-stage continental rift: Constraints from P wave anisotropic tomography. *Tectonics*, *39*(2), e2019TC005590. https://doi.org/10.1029/2019tc005590

Yuan, H., & Bodin, T. (2018). A probabilistic shear wave velocity model of the crust in the central west Australian craton constrained by transdimensional inversion of ambient noise dispersion. *Tectonics*, *37*(7), 1994–2012. https://doi.org/10.1029/2017tc004834

Zhou, L., Xie, J., Shen, W., Zheng, Y., Yang, Y., Shi, H., & Ritzwoller, M. H. (2012). The structure of the crust and uppermost mantle beneath south China from ambient noise and earthquake tomography. *Geophysical Journal International*, *189*(3), 1565–1583. https://doi.org/10.1111/j.1365-246x.2012.05423.x

Zoback, M. L., & Mooney, W. D. (2003). Lithospheric buoyancy and continental intraplate stresses. *International Geology Review*, *45*(2), 95–118. https://doi.org/10.2747/0020-6814.45.2.95

Zulfakriza, Z., Saygin, E., Cummins, P. R., Widiyantoro, S., Nugraha, A. D., Lühr, B.-G., & Bodin, T. (2014). Upper crustal structure of central java, Indonesia, from transdimensional seismic ambient noise tomography. *Geophysical Journal International*, *197*(1), 630–635. https://doi.org/10.1093/gji/ggu016